이학박사학위논문

열대 저기압에 앞서 발생하는 이전 중층 전선에 관한 연구

Antecedent Midtropospheric Frontogenesis ahead of Tropical Cyclone

2014년 2월

서울대학교 대학원

지구환경과학부

백 은 혁

열대 저기압에 앞서 발생하는
이전 중층 전선에관한 연구
Antecedent Midtropospheric Frontogenesis ahead of Tropical Cyclone

지도교수 임 규 호

이 논문을 이학박사 학위논문으로 제출함
2014년 12월

서울대학교 대학원
지구환경과학부
백 은 혁

우 성 호의 이학박사 학위논문을 인준함
2014년 2월

위 원 장 _____ (인)
부위원장 _____ (인)
위 원 _____ (인)
위 원 _____ (인)
위 원 _____ (인)

Abstract

In this study, we demonstrate that the antecedent midtropospheric frontogenesis (AMF) occurred across the middle part of the Korean Peninsula and contributed to the antecedent indirect precipitation (AIP) ahead of TC. We carried out 3 research topics, i.e., case study, comparison study, and statistical analysis.

First, we examined AMF resulting from the interaction between Typhoon Rusa (2002) and a midlatitude trough over the Korean Peninsula. In this event, the AMF contributed to the first peak in the time series of rainfall in Gangneung (37.75°N, 128.90°E), occurring about 12 hours before the landfall of the tropical cyclone (TC). A Weather Research Forecasting (WRF) model experiment revealed that the AMF was mainly forced by the horizontal deformation frontogenetical forcing (HDF). The HDF increased positively due to the confluence of the southeasterlies from the TC and the northwesterlies emanating from the midlatitude trough.

Second, we also investigated favorable synoptic environments for the AIP through comparison of two TCs, Rammasun (2002) and Maemi (2003). Although both had a remarkably similar accumulated rainfall pattern over the peninsula, the temporal evolutions of hourly rainfall were different. Only Maemi had the AIP in conjunction with a midlatitude trough to its north. The confluent flows at middle-to-upper levels were strengthened due to the increased pressure gradient between the midlatitude trough and the subtropical high, and the warm advection by the confluent flows also became stronger near the confluent zone. The highly baroclinic synoptic backgrounds in the Maemi case lead to the AMF.

Finally, we found that many cases showed AIP associated with TCs that were

approaching the Korean Peninsula. In order to generalize the characteristics of the AIP occurrence, we collected all the TC cases that influenced the Korean Peninsula and classified them into two groups depending on the presence of the AIP over the Korean Peninsula. It is found that the AIP cases occur more frequently (about 58% of the total 41 TCs that influenced Korea from 1993 to 2004) than the non-AIP cases and the averaged rain rate of the AIP is about 115 mm $6h^{-1}$. Composite analyses demonstrated that the AIP events tend to be coherent with AMF induced by TC-midlatitude environment interaction. Analysis of the (quasi-geostrophic) QG omega equation indicates that QG forcing, which is related to the AMF, significantly contributes to the ascending motion of the AIP. The AMF was associated with a thermally direct circulation that contributed to strong ascent and the AIP over the peninsula ahead of TC. Moreover, the AIP could intensify due to the abundant low-level moisture supply to the frontal zone by the southerly wind on the east side of the TC.

Key words: Tropical cyclone, typhoon, heavy rainfall, antecedent indirect precipitation, midtropospheric frontogenesis, thermally direct circulation

Student Number: 2002-20586

Table of Contents

1. Motivation and Objectives

Landfall of a tropical cyclone (TC) often causes severe damage to the East Asian regions due to heavy rainfall, strong winds, and storm surges. Predicting the exact location of a landfall is the primary object of real-time monitoring of TCs. They usually accompanied heavy rainfall caused by convection motions inside them. Sometimes, we can expect indirect precipitation developed by their interactions with midlatitude synoptic waves. Because East Asia lies in the midlatitude where many synoptic waves move along the storm track, a TC that develops in the Northwestern Pacific has a high chance of encountering synoptic waves when it moves poleward. When a TC enters a highly baroclinic environment in the midlatitude, its characteristics undergo a change by interacting with the environmental flows. This interaction is termed the extratropical transition (ET) of TC (e.g., Klein et al. 2000; Jones et al. 2003).

The literature on the topic of the interaction between the TC and the midlatitude baroclinic environment may be categorized into two groups. The first group focuses on the ET process in the midlatitude baroclinic environment (e.g., Klein et al. 2000; Harr and Elsberry 2000; Hanley et al. 2001; Sinclair 2002, 2004; Jones et al. 2003; Ritchie and Elsberry 2003, 2007; Harr et al. 2008; Anwender et al. 2008). Klein et al. (2000) defined a conceptual model of ET in terms of two stages (i.e., transformation and reintensification) based on satellite images. Harr and Elsberry (2000) examined the structural characteristics of extratropical cyclones resulting from the ET of Typhoons David and Opal in 1997. Ritchie and Elsberry (2003, 2007) stated that the strength of

the upper-level trough has an impact on the rate of reintensification and phasing between the two has an impact on the peak intensity of the extratropical cyclone. Hanley et al. (2001) reported that about 70% of hurricanes having interacted with an upper-tropospheric trough deepened in the Atlantic. Recently, an ensemble forecast system was employed to examine the predictability of ET process and further downstream circulations (Harr et al. 2008; Anwender et al. 2008).

The second group focuses on the antecedent rainfall ahead of TC (e.g., Bosart and Carr 1978; Stohl et al. 2008; Srock and Bosart 2009; Wang et al. 2009; Chen et al. 2010; Galarneau et al. 2010; Schumacher et al. 2011). Numerous case studies have been carried out to understand the spatio-temporal distribution and intensity of the antecedent rainfall associated with a TC. Bosart and Carr (1978) introduced the antecedent rainfall event ahead of TC Agnes (1972). Since then, numerous studies have reported relevant events. Stohl et al. (2008) described that the transport of tropical and subtropical moisture by two TCs, Maria and Nate (2005) that underwent ET triggered extreme precipitation around the Norwegian southwest coast. Srock and Bosart (2009) examined antecedent rainfall ahead of TC Marco (1990) and presented that the coastal front on the ocean ward edge of the cool pool formed by terrain was responsible for the ascent and precipitation. With two sensitivity experiments (i.e., with a bogus vortex vs. without the TC-related vortex), Wang et al. (2009) attributed the enhancement of remote rainfall in Japan ahead of Typhoon Songda (2004) to northward moisture transport by the TC's outer circulation. Since then, Schumacher et al. (2011) quantified the effect of tropical moisture from TC Erin (2007) on the PRE over Minnesota and

Wisconsin through a sensitivity experiment by removing the moisture transport in a numerical model. These two studies noted that deep tropical moisture is transported to the poleward side of the TC and is forced to ascend when it encounters a low-level baroclinic zone.

Recently, several composite analyses have been conducted over the Atlantic and the western North Pacific. For the Atlantic TCs, Galarneau et al. (2010) defined the PRE as heavy rainfall that occurred well in advance of recurving TCs. The authors analyzed its statistical characteristics, noting that deep tropical moisture is transported well poleward of the TC, which is forced to ascend when encountering a low-level baroclinic zone induced by low-level frontogenetical forcing. For the western North Pacific TCs, Chen et al. (2010) classified the precipitation patterns related with landfalling TCs in China into five categories according to precipitation regions. Among the categories, heavy rainfall in front of the midlatitude trough is called "remote rainfall." Byun and Lee (2012) examined remote effects of TC on the indirect precipitation over the Korean Peninsula through a composite analysis of 46 cases over 29 years (1981–2009). The two studies also suggested that the remote rainfall on the downstream side of the westerly trough is closely related to moisture transport by the strong southeasterly flow in the eastern periphery of the TC.

In this study, we demonstrate that the frontogenesis occurred across the middle part of the Korean Peninsula with its maxima at the mid-level and contributed to the antecedent indirect precipitation (AIP) ahead of TC. For the objective, we carried out 3 research topics, i.e., case study, comparison study, and statistical analysis. First, we

examined antecedent midtropospheric frontogenesis (AMF) resulting from the interaction between Typhoon Rusa (2002) and a midlatitude trough over the Korean Peninsula. In this event, the AMF contributed to the first peak in the time series of rainfall in Gangneung (37.75°N, 128.90°E), occurring about 12 hours before the time of the extratropical transition (ET) process of the tropical cyclone (TC). Second, we also investigated favorable synoptic environments for AIP ahead of TC through comparison of two TCs, Rammasun (2002) and Maemi (2003). Although both had a similar accumulated rainfall pattern over the peninsula, the temporal evolutions of hourly rainfall were different. Only Maemi had the AIP in conjunction with a midlatitude trough to its north. Finally, we found that many cases showed double precipitation peaks, including the AIP, associated with TCs that were approaching the Korean Peninsula. In order to generalize the characteristics of the AIP occurrence, we collected all the TC cases that influenced the Korean Peninsula and classified them into two groups depending on the presence of the AIP over the Korean Peninsula. The composite analyses show how the TC-midlatitude interaction leads to frontogenesis and resultant AIP.

2. Datasets and Methodology

2.1 Datasets

This study uses the gridded dataset of Final global analysis (FNL) produced by National Centers for Environmental Prediction (NCEP) with conducting Global Forecast System (GFS) to diagnose the synoptic-scale environment for Typhoon Rusa (2002) and to use an initial and boundary data of the WRF model for case study. The data set included the horizontal resolution of 1 degree in latitude and longitude and 26 standard pressure levels from 1000 to 10hPa. The data were released from 1999 to present at 6-hourly intervals. However, we use "Japanese 25-year Reanalysis (JRA-25)" to diagnose the synoptic environment associated with each typhoon case for statistical analysis. Because JRA-25 has many advantages to study typhoon-related phenomena, that is, JRA-25 is produced with the assimilation of wind profiles around tropical cyclones reconstructed from historical best track information (Onogi et al., 2007). The horizontal resolution of the JRA-25 is 1.25 degree in latitude and longitude, provided on 23 standard pressure levels from 1000 hPa up to 10 hPa. The data period covers from 1979 to the present at 6-hr intervals.

2011 "Typhoon White Book" issued by the Korea Meteorological Administration (KMA) gives the information of maximum wind speed and direction, maximum daily precipitation, and accumulated precipitation for each surface-based station as well as a track related to typhoons which influenced on the Korean peninsula from 1904 to 2009.

In this study, a set of 22 cases, in which any of Korean surface stations recorded more than 100 mm of the total accumulated precipitation during the influence period of typhoon, is selected from 1993 to 2004 (2011 Typhoon White Book) (Table 5-1). Enhanced infrared satellite imagery from Geostationary Meteorological Satellite (GMS) provided by KMA is used to examine the large-scale cloud features. They are geostationary satellites which provide coverage for the hemisphere centered on 140°E. The hourly precipitation data provided by KMA based on observation at surface stations are also used to examine evolution of heavy rainfall region. In addition, the 3-hourly rain rate data with the 0.25° × 0.25° grid spacing from the Tropical Rainfall Measuring Mission (TRMM) Algorithm 3B42 are examined for the precipitation pattern with a wider scope including the surrounding seas (Huffman et al. 2007). The Best Track data created by the Regional Specialized Meteorological Center (RSMC) Tokyo-Typhoon Center include center positions, maximum wind speeds, and minimum pressures basically at 3-hour intervals from generation to dissipation of Typhoons. Vertical soundings of global stations were obtained from the web site of the department of atmospheric science of University of Wyoming in USA (http://weather.uwyo.edu/upperair/sounding.html).

2.2 WRF Model

For the case study of Typhoon Rusa, given that a front has a short life time (~12 hours to days) and tends to have a narrow swath of precipitation, the research dealing

with a front-induced phenomenon needs data with high spatial and temporal resolutions. A mesoscale numerical model is an appropriate tool to simulate the frontogenesis and its associated phenomena. The Advanced Research Weather Research and Forecasting (WRF/ARW) Model version 3.4 (Skamarock et al. 2008) is employed to reproduce the heavy rainfall event associated with Typhoon Rusa on August 31, 2002. The WRF/ARW model is a fully compressible, non-hydrostatic, primitive equation model with the multiple-nesting capability to zoom in to the area of interest with a higher resolution.

Initial and lateral boundary conditions are taken from the NCEP FNL data from 00 UTC 29 August to 00 UTC 01 September 2002 with 6-hourly intervals. Three domains are respectively configured with horizontal resolutions of 27 km, 9 km and 3 km, keeping their centers at Gangneung (37.75°N, 128.90°E). Fig. 2-1 illustrates the model domain setting for this study. Domain 1 (D01) is the mother (outermost) domain with 180 × 180 grid points, and domains 2 (D02) and 3 (D03) are the nested (inner) domains with 360 × 360 and 720 × 720 grid points, respectively. The three domains are identically set up with 34 vertical layers with the model top at 50 hPa. The initial times for D01, D02, and D03 are 00 UTC 29, 12 UTC 29 and 00 UTC 30 August, respectively, in which a 12-hr spin-up time of the coarser domain is set to run the finer domain. Time steps for the model integration are 180s for D01, 60s for D02 and 20s for D03. All domains are provided with two-way nesting method for feedback to occur between the coarse-resolution domain and the nest throughout the simulation. In Fig. 2-1, the terrain height is shown for D03. The Korean Peninsula has a long mountain

range called the Taebaek Mountain Range (TMR) running along the east coast of the peninsula together with Jiri Mountain located in the south-central part of the peninsula.

The model physics used are as follows: The Kain-Fritsch cumulus parameterization scheme (Kain and Fritsch 1993) is used for subgrid-scale deep convection on D01 and D02, whereas cumulus parameterization is turned off for D03. For the moist processes of grid-scale clouds and precipitation, we use the WRF single-moment six-class microphysics scheme (WSM6) (Hong et al. 2004; Hong and Lim 2006). Besides, we use the Yonsei University (YSU) scheme (Hong et al. 2006) for the planetary boundary layer, the Noah land surface model (Chen and Dudhia 2001) for the land surface, and the rapid radiative transfer model (RRTM) longwave scheme (Mlawer et al. 1997) together with the Dudhia shortwave scheme (Dudhia 1989) for atmospheric radiation processes. Note that we use the same physics schemes as those of Lee and Choi (2010) because they verified the validity of those schemes in their analysis of the effects of Typhoon Rusa over the Korean Peninsula.

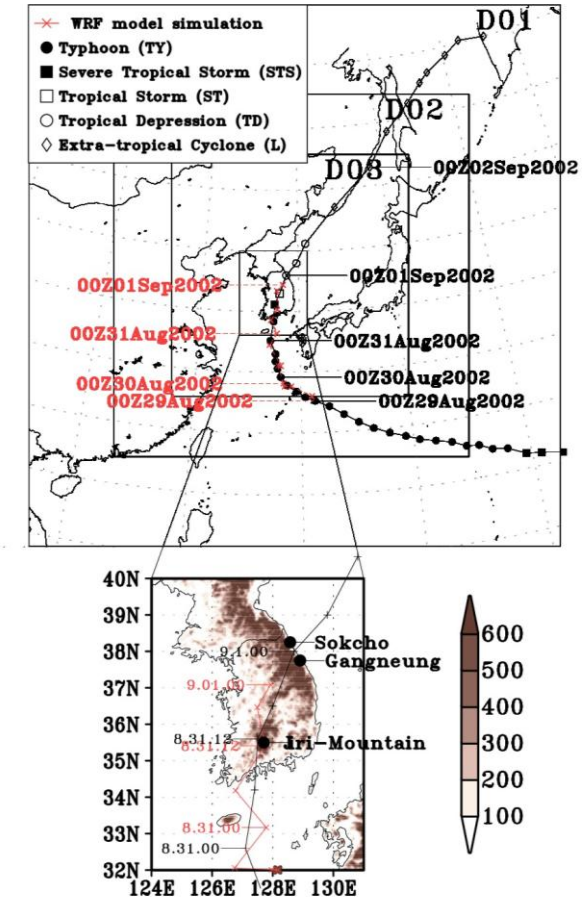

Fig. 2-1. The track and intensity of Typhoon Rusa over the period from 00 UTC 25 August to 00 UTC 2 September 2002 as designated by the RSMC best track data (black line) and the track simulated by domain 1 (red dotted line) of the WRF/ARW model during model integration time from 00 UTC 29 August to 00 UTC 1 September (upper figure). The central positions are marked every six hours. The WRF/ARW model domain 1 (D01), 2 (D02), and 3 (D03) are delineated as well. The bottom figure shows zoomed tracks and terrain heights (m) of domain 3 together with locations of Gangneung, Sokcho, Jiri-Mountain, and Taebaek Mountain Range (TMR).

2.3 Frontogenesis Function

For the case and comparison study, frontogenesis function was used to diagnose the evolution and development of the front between Typhoon and the middle latitude trough at mid-troposphere. Atmospheric frontogenesis was defined by Petterssen (1936) as the Lagrangian rate of change of the magnitude of the horizontal potential-temperature (θ) gradient due to the horizontal wind ($\mathbf{V}_{\mathrm{H}} = u\mathbf{i} + v\mathbf{i}$) which is related to horizontal divergence and resultant deformation. As extended definition by Miller (1948) for a front in free atmosphere, frontogenesis is the Lagrangian rate of change of the magnitude of the three-dimensional gradient of the potential temperature (θ) due to the three-dimensional wind ($\mathbf{V} = u\mathbf{i} + v\mathbf{j} + \omega\mathbf{k}$) in ($x, y, p$) coordinates. After that, the concept of frontogenesis function was expressed as various formulas as an intention of researcher. Keyser et al. (1988) analyzed the changes in the temperature field in terms of the vector frontogenesis function that consists of scalar and rotational contributions to frontogenesis. Scalar frontogenesis acts to change the magnitude of the potential temperature gradient while rotational frontogenesis acts to rotate the potential temperature gradient. Schultz and Doswell (1999) modified the formulation to include the frontogenetical effects due to gradients of vertical motion. In this paper, we wish to understand the evolution of a mid-level front due to the interaction between Typhoon and a middle latitude trough, so that the frontogenetical effects due to not only gradients of vertical motion but also diabatic forcing generated by latent heat exchange of the northern part of Typhoon should be considered. Therefore we define

frontogenesis, F as the Lagrangian rate of change of the magnitude of the horizontal potential temperature gradient due to the three-dimensional wind with diabatic forcing:

$$\mathrm{F} \equiv \frac{D}{Dt} | \nabla_H \theta | \quad (1),$$

where

$$\frac{D}{Dt} = \frac{\partial}{\partial t} + u \frac{\partial}{\partial x_p} + v \frac{\partial}{\partial y_p} + \omega \frac{\partial}{\partial p}$$

$$\nabla_H = \mathbf{i} \frac{\partial}{\partial x_p} + \mathbf{j} \frac{\partial}{\partial y_p} .$$

The subscript p indicates differentiation on an isobaric surface and hereafter will be implicit in this section. In this study, the thermodynamic equation was not conserved in the frontogenesis function formula in order to consider the diabatic forcing. Thus we calculated Lagrangian rate of the potential temperature with repect to time to obtain the diabatic forcing by using to following expression:

$$\frac{D\theta}{Dt} = \frac{\partial\theta}{\partial t} + u\frac{\partial\theta}{\partial x} + v\frac{\partial\theta}{\partial y} + \omega\frac{\partial\theta}{\partial p} = \left(\frac{p_0}{p}\right)^{\kappa}\frac{1}{C_p}\frac{dQ}{dt} \qquad (2)$$

where $\kappa = R/C_p$ and dQ/dt include latent heat exchange and radiation. Differentiating the equation of three-dimensional diabatic flow, respectively by x and y, defines the components of (1):

$$\frac{D}{Dt}\left(\frac{\partial\theta}{\partial x}\right) = \frac{1}{C_p}\left(\frac{p_0}{p}\right)^{\kappa}\left[\frac{\partial}{\partial x}\left(\frac{dQ}{dt}\right)\right] - \frac{\partial u}{\partial x}\frac{\partial\theta}{\partial x} - \frac{\partial v}{\partial x}\frac{\partial\theta}{\partial y} - \frac{\partial\omega}{\partial x}\frac{\partial\theta}{\partial p} \qquad (3a)$$

$$\frac{D}{Dt}\left(\frac{\partial\theta}{\partial x}\right) = \frac{1}{C_p}\left(\frac{p_0}{p}\right)^{\kappa}\left[\frac{\partial}{\partial y}\left(\frac{dQ}{dt}\right)\right] - \frac{\partial u}{\partial y}\frac{\partial\theta}{\partial x} - \frac{\partial v}{\partial y}\frac{\partial\theta}{\partial y} - \frac{\partial\omega}{\partial y}\frac{\partial\theta}{\partial p} \qquad (3b)$$

Combination of (3a) and (3b) provides the following expressions for the three-dimensional frontogenesis function of the horizontal gradient of the potential temperature:

$$F_H = \frac{1}{|\nabla_H \theta|}\left\{\begin{array}{l} \dfrac{\partial\theta}{\partial x}\left\{\dfrac{1}{C_p}\left(\dfrac{p_0}{p}\right)^{\kappa}\left[\dfrac{\partial}{\partial x}\left(\dfrac{dQ}{dt}\right)\right]-\left(\dfrac{\partial u}{\partial x}\dfrac{\partial\theta}{\partial x}\right)-\left(\dfrac{\partial v}{\partial x}\dfrac{\partial\theta}{\partial y}\right)-\left(\dfrac{\partial\omega}{\partial x}\dfrac{\partial\theta}{\partial p}\right)\right\} \\ +\dfrac{\partial\theta}{\partial y}\left\{\dfrac{1}{C_p}\left(\dfrac{p_0}{p}\right)^{\kappa}\left[\dfrac{\partial}{\partial y}\left(\dfrac{dQ}{dt}\right)\right]-\left(\dfrac{\partial u}{\partial y}\dfrac{\partial\theta}{\partial x}\right)-\left(\dfrac{\partial v}{\partial y}\dfrac{\partial\theta}{\partial y}\right)-\left(\dfrac{\partial\omega}{\partial y}\dfrac{\partial\theta}{\partial p}\right)\right\} \end{array}\right\} \quad (4)$$

Finally the frontogenetical forcing terms were relocated into the each physical sense grouping with substituting eq. (2) as following expressions.

$$F_H \equiv \frac{d\left|\nabla_H\theta\right|}{dt} = \frac{1}{\left|\nabla_H\theta\right|}\left\{\begin{array}{l} \underbrace{\dfrac{\partial\theta}{\partial x}\left(-\dfrac{\partial u}{\partial x}\dfrac{\partial\theta}{\partial x}-\dfrac{\partial v}{\partial x}\dfrac{\partial\theta}{\partial y}\right)+\dfrac{\partial\theta}{\partial y}\left(-\dfrac{\partial u}{\partial y}\dfrac{\partial\theta}{\partial x}-\dfrac{\partial v}{\partial y}\dfrac{\partial\theta}{\partial y}\right)}_{HDF} \\ \underbrace{+\dfrac{\partial\theta}{\partial p}\left(-\dfrac{\partial\varpi}{\partial x}\dfrac{\partial\theta}{\partial x}-\dfrac{\partial\varpi}{\partial y}\dfrac{\partial\theta}{\partial y}\right)}_{TF}+\underbrace{\dfrac{\partial\theta}{\partial x}\left[\dfrac{\partial}{\partial x}\left(\dfrac{D\theta}{Dt}\right)\right]+\dfrac{\partial\theta}{\partial y}\left[\dfrac{\partial}{\partial y}\left(\dfrac{D\theta}{Dt}\right)\right]}_{DF} \end{array}\right\} \quad (5),$$

where, ∇_H, θ, u, v, and ϖ are the horizontal gradient, potential temperature, zonal wind, meridional wind, and pressure velocity, respectively. On the right-hand side of Eq. (5), the first four terms constitute the horizontal deformation forcing (HDF), the next two terms indicate the tilting forcing (TF), and the last two terms denote the diabatic forcing (DF).

2.4 QG Analysis

For the composite study, Quasi-geostrophic (QG) dynamics is applied to assess the role of midtropospheric front in ascent for the AIP cases. The QG frontogenesis function, F_g, is described by the following equation:

$$F_g = \frac{d_g}{d}\left|\nabla_p \theta\right| = \frac{1}{\left|\nabla_p \theta\right|}\left[-\frac{\partial \theta}{\partial x}\left(\frac{\partial u_g}{\partial x}\frac{\partial \theta}{\partial x}+\frac{\partial v_g}{\partial x}\frac{\partial \theta}{\partial y}\right)-\frac{\partial \theta}{\partial y}\left(\frac{\partial u_g}{\partial y}\frac{\partial \theta}{\partial x}+\frac{\partial v_g}{\partial y}\frac{\partial \theta}{\partial y}\right)\right] \quad (6)$$

where, $\frac{d_g}{dt} = \frac{\partial}{\partial t} + u_g\frac{\partial}{\partial x} + v_g\frac{\partial}{\partial y}$.

The frontogenesis function could be rewritten by the Q-vector form:

$$F_g = \frac{1}{\left|\nabla_p \theta\right|}\vec{Q}\cdot\nabla_p\theta \quad (7)$$

where $\vec{Q} = \frac{d_g}{dt}\nabla_p\theta = \left[-\left(\frac{\partial u_g}{\partial x}\frac{\partial \theta}{\partial x}+\frac{\partial v_g}{\partial x}\frac{\partial \theta}{\partial y}\right),-\left(\frac{\partial u_g}{\partial y}\frac{\partial \theta}{\partial x}+\frac{\partial v_g}{\partial y}\frac{\partial \theta}{\partial y}\right)\right]$.

From (7), a positive value of F_g indicates that the Q vector would be oriented toward the warm side of a frontogenetic region and a thermally direct circulation would be induced (e.g., Martin et al. 1992).

We also calculated each term of the QG omega equation to assess quantitatively the role of QG frontal forcing. The following equation describes the QG omega equation for frictionless atmosphere:

$$\left(\nabla^2 + \frac{{f_0}^2}{\sigma}\frac{\partial^2}{\partial p^2}\right)\omega = -\frac{f_0}{\sigma}\frac{\partial}{\partial p}\left[-\vec{V}_g \cdot \nabla\left(\frac{1}{f_0}\nabla^2\Phi + f\right)\right] - \frac{1}{\sigma}\nabla^2\left[-\vec{V}_g \cdot \nabla\left(-\frac{\partial\Phi}{\partial p}\right)\right] - \frac{R}{\sigma p}\nabla^2\left(\frac{1}{C_p}\frac{dQ}{dt}\right) \quad (8)$$

There are three forcing terms on the right-hand side of (8), they respectively represent the differential geostrophic vorticity advection, the Laplacian of potential temperature advection, and the Laplacian of diabatic heating. In the third term, the diabatic heating can be computed as a residual from the thermodynamic equation. However, the calculation of Eulerian derivatives using the JRA-25 data with 6-hr time interval brings about large computational residuals because of the coarse temporal resolution of the data (Moore and Montgomery 2005). To avoid this problem, computing the diabatic heating from 3-dimensional air parcel trajectories has been proposed to minimize the computational error (e.g., Galarneau et al. 2009; Cordeira and Bosart 2011). We used this Lagrangian method to calculate the diabatic heating of frontogenesis function. The method is described as follows: First, the 6-hourly data is first linearly interpolated to 1-hr interval, and then the Lagrangian derivative of potential temperature at a grid point is computed by the centered finite difference method using two air parcel points–one at 1-hr forward and the other at 1-hr backward trajectory in Eq. (8).

3. Case Study of Typhoon Rusa (2002)

The AIP case in East Asia may be found for the interaction of Typhoon Rusa (2002) with a midlatitude trough prior to its landfall on the Korean Peninsula (Park and Lee 2007; Lee and Choi 2010). The Korean Peninsula was devastated by this TC, mainly due to the associated heavy rainfall. In particular, the daily precipitation reached 870.5 mm day^{-1} in Gangneung (37.75°N, 128.90°E, marked in Fig. 2-1) which is located on the mid-eastern coast of the peninsula. Interestingly, clearly separated double peaks appeared in hourly precipitation time series in Gangneung during the course of TC landfall. Park and Lee (2007) suggested that the enhancement of low-level convergence by prevailing northeasterlies and the strengthening of the outer circulation of Rusa greatly increased the precipitation amount in the region of orographically induced convection. By contrast, Lee and Choi (2010) noted that a mid-tropospheric frontal structure was associated with the first rainfall peak together with the orographic lifting.

In this study, we confirm that the first heavy rainfall period in Gangneung was an AIP event (i.e., PRE) if we take the track and the radius of influence of Rusa into account. Previous studies discussed two mechanisms (orographic lifting and frontogenetical forcing) pertaining to this event. To understand the AIP associated with Rusa, we investigate the relative importance of orographic lifting and frontogenetical forcing using high-resolution numerical modeling. How the frontogenesis was formed by the TC–environment interaction process before the commencement of the ET

process is also examined through the detailed budget analysis of the frontogenesis function. Particularly, we demonstrate that the frontogenesis occurred across the middle part of the Korean Peninsula with its maxima at the mid-level and contributed to the first rainfall event in Gangneung.

3.1 Typhoon Rusa

Typhoon Rusa (2002) started in the tropical mid-Pacific Ocean. According to the RSMC best-track record, it reached tropical depression status at 06 UTC 22 August and obtained the strength of tropical storm at 00 UTC 23 August at 16.5°N, 161.0°E. At 18 UTC 25 August, it headed west-northwestward and reached TC intensity, and it gradually turned north over the East China Sea about 350 km southwest of Kagoshima of Japan (29.6°N, 128.1°E) at 00 UTC 30 August (Fig. 2-1). It made landfall on the south coast (34.4°N, 127.4°E) of the Korean Peninsula around 06 UTC 31 August, with a maximum wind speed of 38 m s−1 and a central minimum pressure of 960 hPa. Rusa kept typhoon intensity until 06 UTC 31 August and then weakened rapidly after it made a landfall on the peninsula. However, it reintensified at 00 UTC 2 September while transforming to an extratropical cyclone.

3.1.1. Heavy rainfall event

While Rusa approached and moved across the peninsula, heavy rainfall occurred in

Gangneung and over Jiri Mountain during 30–31 August (Fig. 3-1). Gangneung received 870.5 mm of accumulated precipitation in a one day, the highest daily total in Korean meteorological history. Two rainfall peaks are conspicuous in the timeseries of hourly amounts of the extreme rainfall in Gangneung (Fig. 3-1b) while a single peak is obvious in Jiri Mountain (Fig. 3-1c). For the Gangneung area, the first and second peaks were respectively recorded with the amounts greater than 60 mm hr−1 at 23 UTC 30 August and 13 UTC 31 August (Fig. 3-1b). The single rainfall peak of about 40 mm hr−1 on Jiri Mountain was recorded at 08 UTC 31 August (Fig. 3-1c). The double-peak pattern in Gangneung is similar to the two distinct rainfall events over the southeast United States associated with Atlantic Tropical Storm Marco (1990) as shown by Srock and Bosart (2009) (See their Fig. 4).

The accumulated amount of precipitation during 30–31 August based on the TRMM 3B42 data shows a similar pattern to the surface gauge data, although the amount was rather small corresponding to about 30% of that of the surface gauge data (Fig. 3-2a). The accumulated amount of precipitation from 21 UTC 30 to 00 UTC 31 August (within the first rainfall peak) shows two rain shields; one is located over the northern sector of Rusa within its effective zone (black circle in Fig. 3-2b) which is defined as the radius of wind speed 15.4 m s−1 obtained from the RSMC Tokyo best track dataset, and the other is ahead of the TC from the middle part of the peninsula to the northeast across Gangneung (Fig. 3-2b). The latter appears to be an antecedent precipitation (i.e., a PRE-type), which could be separated from rainfall within the Rusa's sphere of direct influence. For the remainder of this study, we will focus on the

synoptic features of the first AIP in Gangneung and the relevant mechanism producing the rainfall.

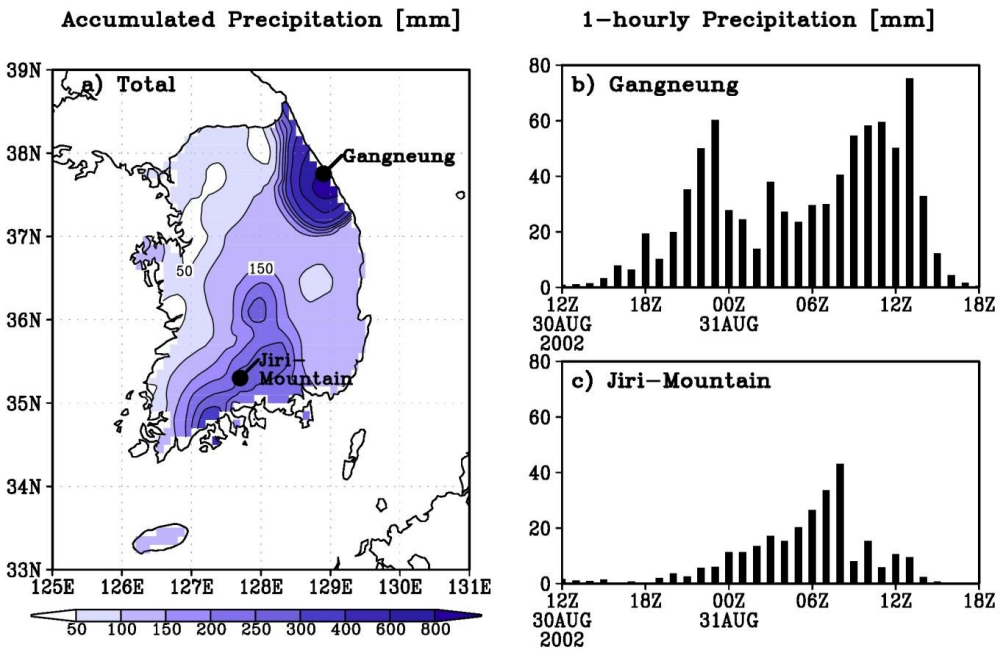

Fig. 3-1. (a) Total precipitation (mm) and time series of hourly precipitation (mm) at (b) Gangneung and (c) Jiri-Mountain, observed in weather stations in the Korean Peninsula from 12 UTC 30 August to 18 UTC 31 August 2002.

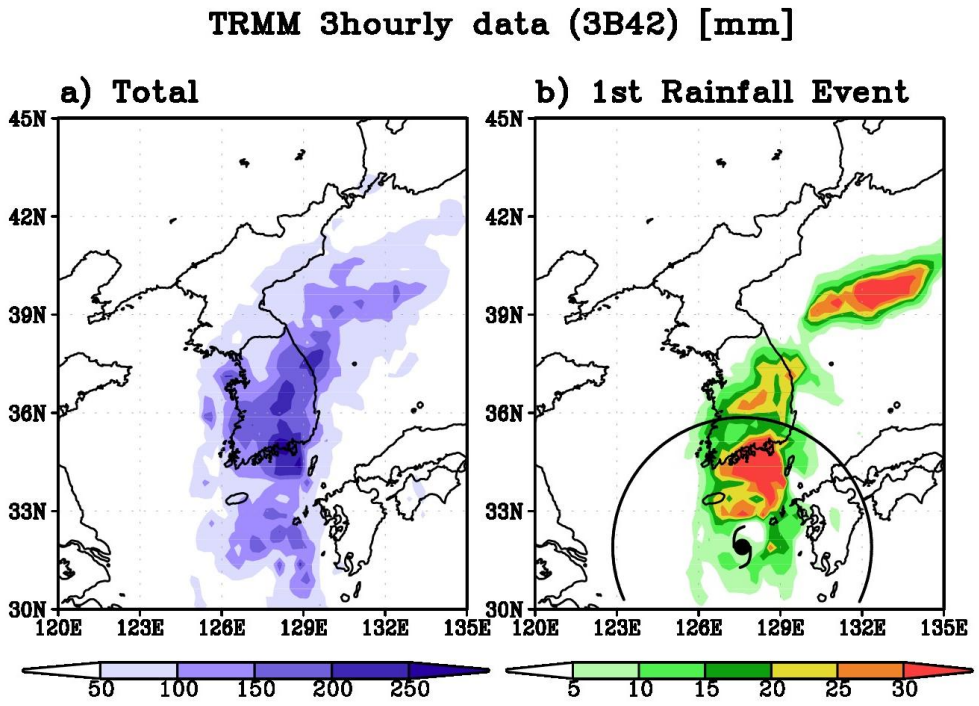

Fig. 3-2. (a) Total precipitation (mm) integrated from 12 UTC 30 August through 00 UTC 1 September 2002 and (b) 3-hr accumulated precipitation from 21 UTC 30 to 00 UTC 31 August 2002 from the TRMM 3B42 3-hourly rainfall dataset. The circle in (b) denotes the effective size (See the text in Section 3.2) at 00 UTC 31 August.

3.1.2. Synoptic environment

Enhanced IR images show the evolution of the convective features associated with Rusa (Fig. 3-3). The first rainfall event in Gangneung occurred from 18 UTC 30 August to 00 UTC 31 August (Figs. 3-4a–3-4c). During this period, a detached region with high cloud-top temperature, i.e., deep convective cloud band was observed to the north of the circular cloud shield around Rusa. Particularly at 21 UTC 30 August, the detached cloud band was evident over the southern part of the peninsula when the first rainfall event in Gangneung reached its maximum (Fig. 3-3b). This horizontal configuration of the deep convection is consistent with that of TRMM rainfall during the first rainfall event (Fig. 3-2b), indicating that the first rainfall event in Gangneung occurred outside of directly influenced region by Rusa. As the TC moved to the north, the cloud shield of Rusa covered the peninsula after 03 UTC 31 August (Figs. 3-4d–3-4f) mostly. Typhoon Rusa made a landfall on the south coast of the peninsula at 06 UTC 31 August, during which the second rainfall event occurred in Gangneung (Fig. 3-3e). After 3 hours, strong convection was located in the central and eastern part of South Korea. During this time period, the second rainfall reached its maximum (Fig. 3-3f).

Fig. 3-4 shows the synoptic environment at the low (850 hPa) and middle-to-upper (500 and 200 hPa) tropospheric levels from the NCEP FNL data as Rusa affected the Korean Peninsula. At 12 UTC 30 August (Figs. 3-5a and 3-5d), the highly humid zone (more than 90%) was confined around the TC, with a moist plume extending along the east coast of the continent between the subtropical high and the anticyclone over

Manchuria. At the midtropospheric level, a midlatitude trough intruded into the northern part of the peninsula, and the upper-tropospheric jet was seen on the downstream side of the midtropospheric trough (Fig. 3-4a).

Figs. 3-4b and 3-4e show the synoptic pattern around the peak time of the first rainfall event (00 UTC 31 August) in Gangneung. The northward extending moist plume was further intensified, and northeasterlies blew perpendicularly to the dilatation of the TMR on the northern periphery of Rusa at the low-level. Deep convection could be enhanced by orographically induced ascending currents on the upwind side of the TMR (Park and Lee 2007; Lee and Choi 2010). At 500 hPa, the southerlies on the eastern flank of Rusa come across the midlatitude westerlies of the pre-existing trough (Fig. 3-4e). A horizontal confluent deformation field was thus enhanced across the middle part of the peninsula, where the warm and moist air met with the cold and dry air (Lee and Choi 2010). This condition was in good agreement with a frontogenesis process; i.e., an enhanced temperature gradient. The upper-tropospheric jet intensified over the northeast of the peninsula in relation with the enhanced vertical wind shear. Most of the Korean peninsula was under the direct influence of Rusa by 12 UTC 31 August (Figs. 3-5c and 3-5f). The cyclonic circulation associated with Rusa prevailed at the low- and midtropospheric levels, and the upper-tropospheric jet was further intensified as the trough moved away from the peninsula. At this time, the second rainfall peak was observed in Gangneung (Fig. 3-1b).

A skew T-log p diagram of sounding data at Sokcho (47090, 38.25°N, 128.57°E, marked in Fig. 2-1) is shown for 18 UTC 30 August (5 hours before the first rainfall

peak in Gangneung) (Fig. 3-5). Sokcho is selected because it is the aerological observatory closest to Gangneung. Saturated layers exist at both low- and mid-troposphere, and the atmosphere was relatively dry between two saturated layers. This suggests that different processes worked on the saturation of the two layers. The lowermost saturation layer below 850 hPa was formed by easterlies which brought abundant moisture to the TMR, which could be sustained by orographic lifting along the slope of the TMR as discussed by Park and Lee (2007) and Lee and Choi (2010). Veering winds with height between 800 and 600 hPa suggest warm air advection and the sudden drop of dew point temperature indicates the intrusion of dry air at this intermediate layer. Above this layer, there was neither strong veering nor backing, but another saturation layer was found. This saturation layer was conditionally stable because the temperature lapse rate was lower than the moist adiabatic lapse rate. It is also notable that the temperature lapse rate abruptly changed in the stable and saturated layer, implying the possible existence of the midtropospheric frontal zone. It is conceived that the warm air would have confronted with the relatively cold air above from the midtropospheric trough, which could intensify the horizontal temperature gradient (i.e., frontogenesis) (see Fig. 3-4).

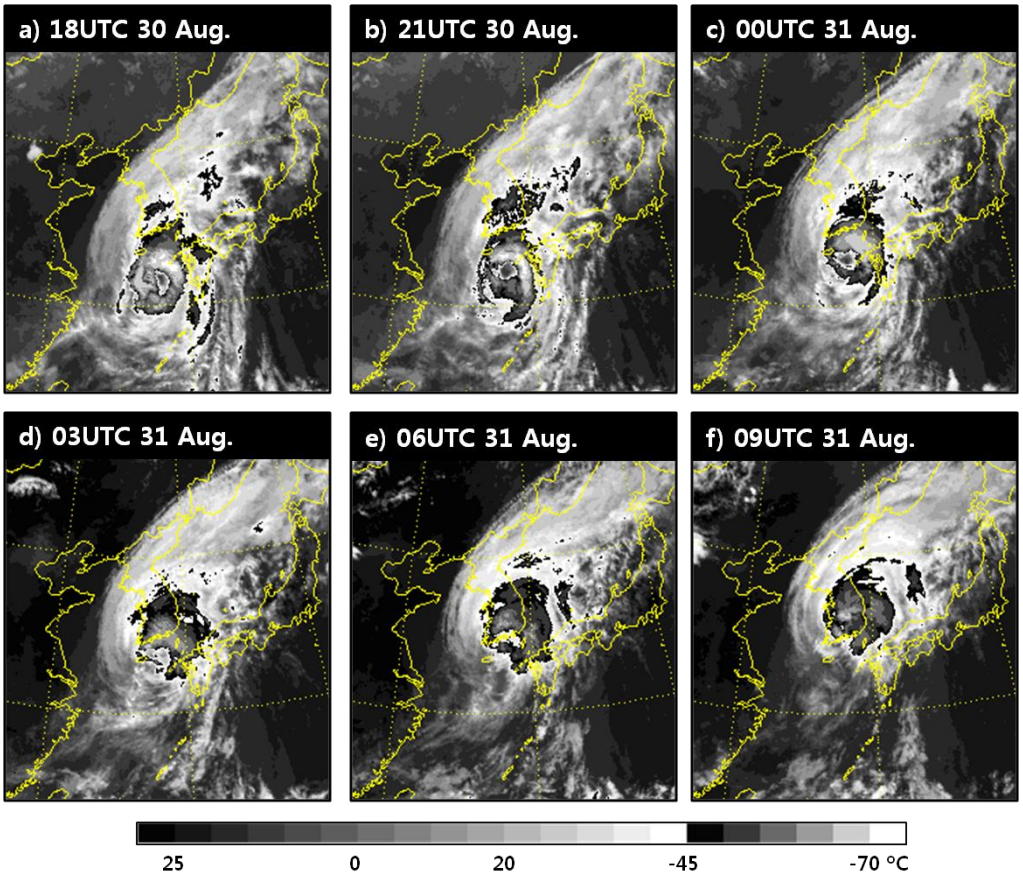

Fig. 3-3. Enhanced IR images from the GMS at (a) 18 UTC 30, (b) 21 UTC 30, (c) 00 UTC 30, (d) 03 UTC, (e) 06 UTC, and (f) 09 UTC 31 August 2002.

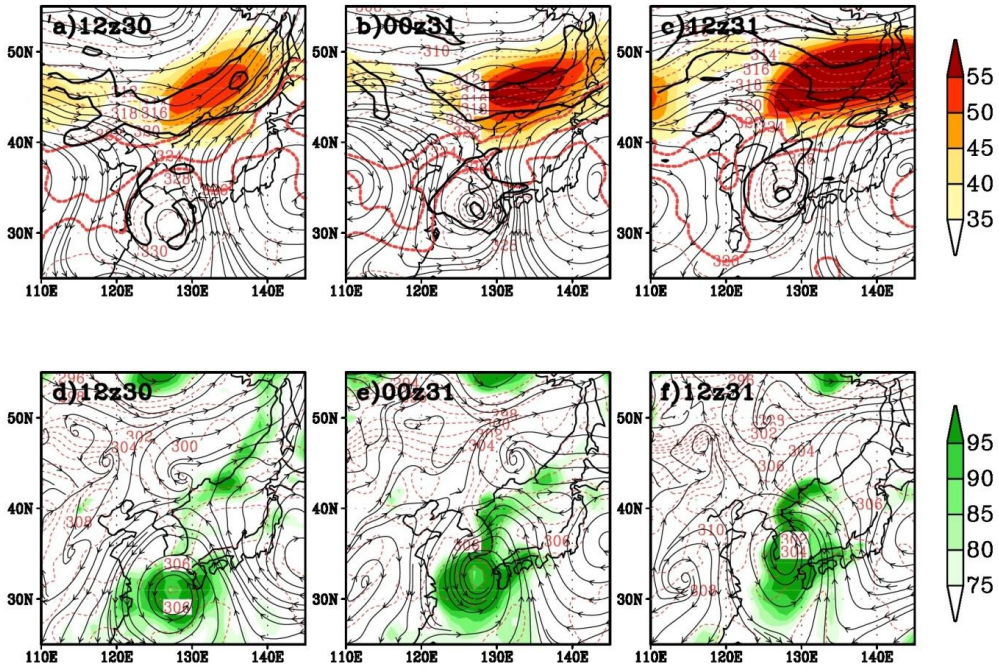

Fig. 3-4. (a) 500-hPa streamlines (black solid), potential temperature (K, red dashed), 1.5 10^{-5} K m^{-1} potential temperature gradient (thick line), and 200-hPa isotachs (m s^{-1}) at 12 UTC 30 August 2002. (d) 850-hPa streamlines (black solid), potential temperature (K, red dashed), and relative humidity (%, shaded) at 12 UTC 30 August 2002. (b,e) and (c,f) as in (a,d) but for 00 UTC 31 and 12 UTC 31 August 2002, respectively.

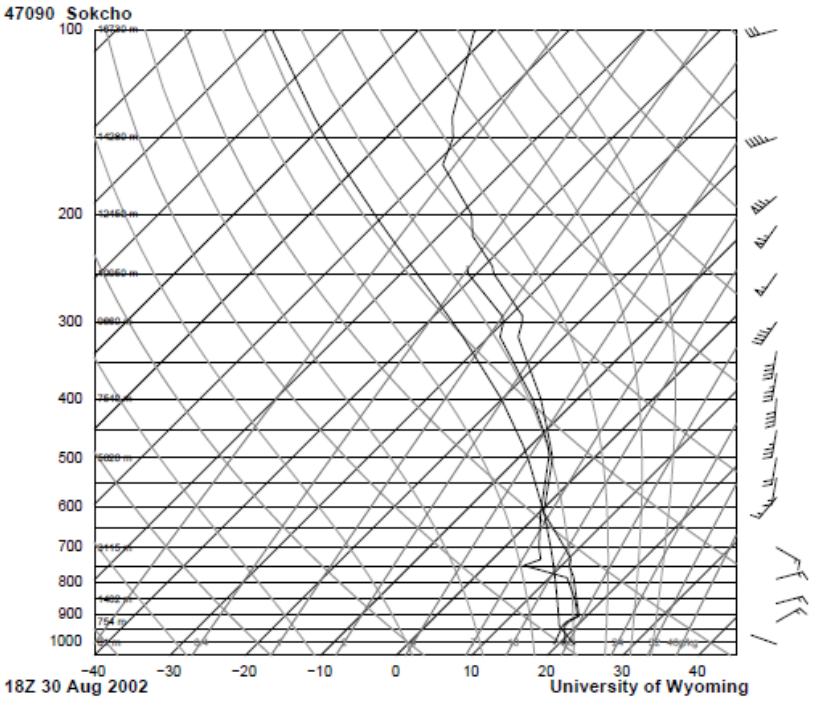

Fig. 3-5. Vertical sounding (skew T-log p diagram) of temperature, dew point temperature, and horizontal winds at 18 UTC 30 August 2002 at Sokcho (47090, [38.25°N, 128.57°E]). (Available via http://weather.uwyo.edu/upperair/sounding.html).

3.2 Midtropospheric frontogenesis

The observational evidences on the midtropospheric saturation suggest the AMF for the first rainfall event in Gangneung. Therefore the AMF deserves to be analyzed more comprehensively using the numerical model. In this section, we aim to answer to the following questions: Why should we note the midtropospheric phenomenon on top of the low-level terrain effect? What forcing causes the frontogenesis? How does the front contribute the first rainfall event?

3.2.1. Validation of the WRF/ARW model simulation

The WRF/ARW model reasonably simulated the atmospheric environments during the integration period, which are similar to their observational counterparts. For example, the simulated temperature and wind fields were similar to those of the reanalysis data at 500 hPa (Figs. 3-5a, b, c vs. Figs. 3-10a, b, c). The observed and D01-simulated tracks of Rusa are presented together. The simulated track was also similar to that from the RSMC best track data, which reveals that the WRF/ARW model is capable of simulating the atmospheric environments relevant to the TC track (Fig. 2-1).

Fig. 3-6 shows the horizontal distributions of the total accumulated rainfall (Fig. 3-6a) and the 3-hr accumulated rainfall (from 21 UTC 30 August to 00 UTC 31 August) within the first rainfall event (Fig. 3-6b), simulated over D03. The total accumulated

precipitation at the maximum grid point was 844.9 mm. Like the observed features (Figs. 3-2 and 3-3), the model reasonably simulated the maximum accumulated rainfall regions over Jiri Mountain and the east side of the TMR (Fig. 3-6a). The 3-hr accumulated rainfall during the first event was also reasonably simulated (Fig. 3-6b). The narrow-banded pattern from the mid-eastern part of the peninsula toward its northeast sea corresponded to the observation (Fig. 3-2b). Fig. 3-6c presents the simulated hourly precipitation at the maximum grid point in Fig. 3-6b near Gangneung over D03. Although the core point along the central east coast was displaced slightly to the northwest (37.93°N, 128.65°E) of Gangneung and the rainfall amount at the first peak is much less than observation, it is noteworthy that the simulated precipitation clearly showed double peaks and recorded the first rainfall peak at 23 UTC 30 August, in accordance with the observation. As the front is a line-shaped phenomenon, it is more natural to pick up meteorological fields following the direction of the frontal line (shown in Figs. 3-8d and 3-10b). Thus, we additionally present the average hourly precipitation in the area (the boxes in Fig. 3-6b) following the direction of the frontal line. The time series still shows the separated peak of the first rainfall event at 23 UTC 30 August, whereas the second event appears to be divided into two due to the relatively stronger suppression of the rainfall amount around 10 UTC 31 August. Based on the time series, we set the analysis time of the model output at 23 UTC 30 August when the first rainfall peak was recorded in both the observation and model.

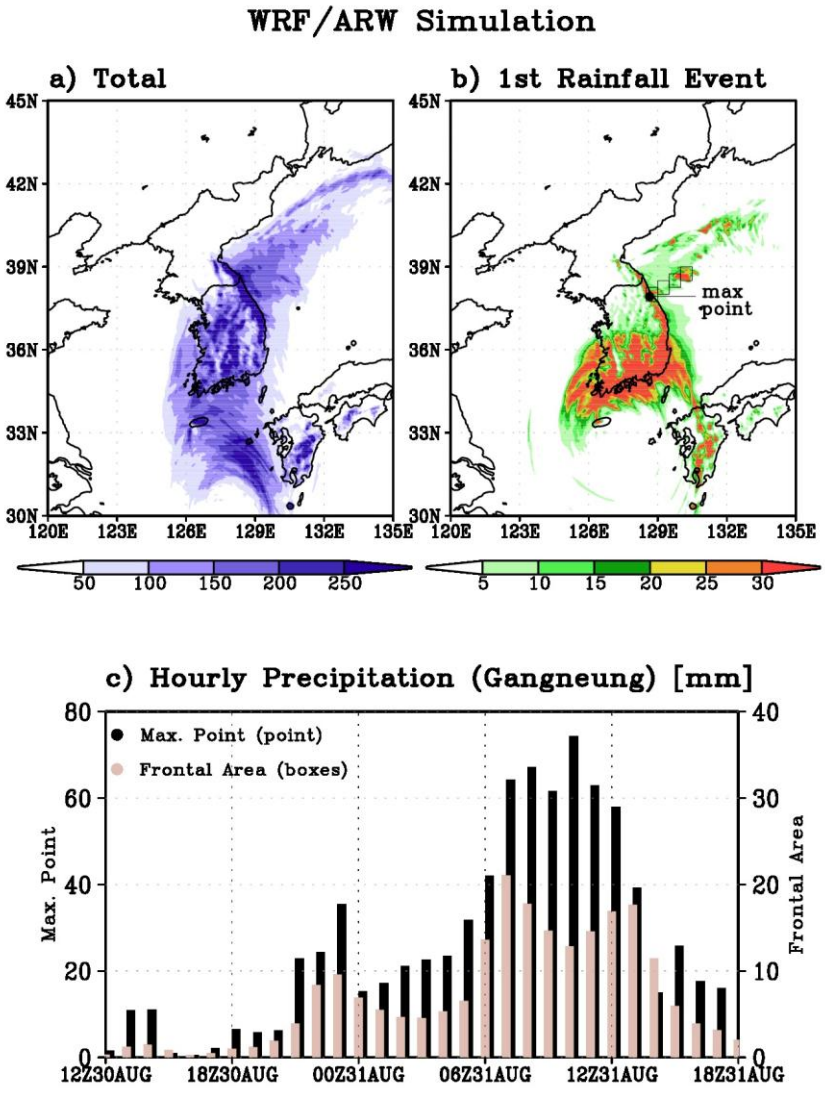

Fig 3-6. (a) The simulated 36-hr accumulated total precipitation (mm) from 12 UTC 30 August to 00 UTC 1 September 2002, (b) the 3-hr accumulated precipitation (mm) from 21 UTC 30 to 00 UTC 31 August 2002, and (c) the time series of hourly precipitation (mm) at the point with maximum total precipitation (the black dot in (b), black bars) and averaged over the frontal regions (4 boxes in (b), pink bars) from D03.

3.2.2. Midtropospheric phenomenon

In both the FNL data and model output, the horizontal gradient of potential temperature was relatively strong from the middle part of the peninsula toward the northeast at 500 hPa at the analysis time (Fig. 3-7), indicating that the WRF/ARW model well simulated the frontal structure. The strong ascent occurred on the warm side of the front away from the deep convection around the TC (Figs. 3-8a and 3-8b). The horizontal distribution of the ascending region is similar to that of the 3-hr accumulated rainfall (Fig. 3-2b) and to the observed cloud shield in the enhanced IR image (Figs. 3-3b and 3-3c). On the other hand, abundant moisture was efficiently transported to the Korean Peninsula by the southerlies on the eastern flank of Rusa at the mid-level (Figs. 3-7c and 3-7d). Deep moisture is a well-known key ingredient for heavy rainfall (Doswell et al. 1996). The moisture flux convergence (MFC) was located along the front due to strong convergence. The combination of the ascending motion and the MFC lead to condensation at the mid-troposphere.

The origins of midtropospheric moisture at the grid points around the maximum precipitation (i.e., Gangneung and Jiri Mountain) were tracked by calculating the 24-hr backward trajectories starting from the time of the first peak with the three-dimensional back-tracking technique (Fig. 3-8a). The trajectories of individual air parcels which were selected at the mid-troposphere presented very different paths between the two regions. Midtropospheric water vapor above Gangneung was transported all the way from the mid-troposphere above the subtropical ocean to the precipitating region by the

southerlies along the eastern periphery of the TC. In contrast, those above Jiri Mountain followed the cyclonic path near the TC center with a strong ascent in one day due to the convective updraft of the TC. The vertical-meridional transports of the air parcel show the distinctive patterns between the low- and mid-level at the maximum precipitation point near Gangneung (Fig. 3-8b). Midtropospheric air parcels above 2 km originated from the mid-troposphere over the East China Sea while the lower-tropospheric air parcels were transported from near-surface over the East/Japan Sea by the northeasterlies orthogonal to the TMR (See Fig. 3-4c). These results suggest that the substantial moist air above the maximum precipitation region came from the mid-troposphere subtropical ocean and was lifted by the midtropospheric forcing. These features indicate that the midtropospheric ascent and saturation above Gangneung were attributed to the frontogenesis.

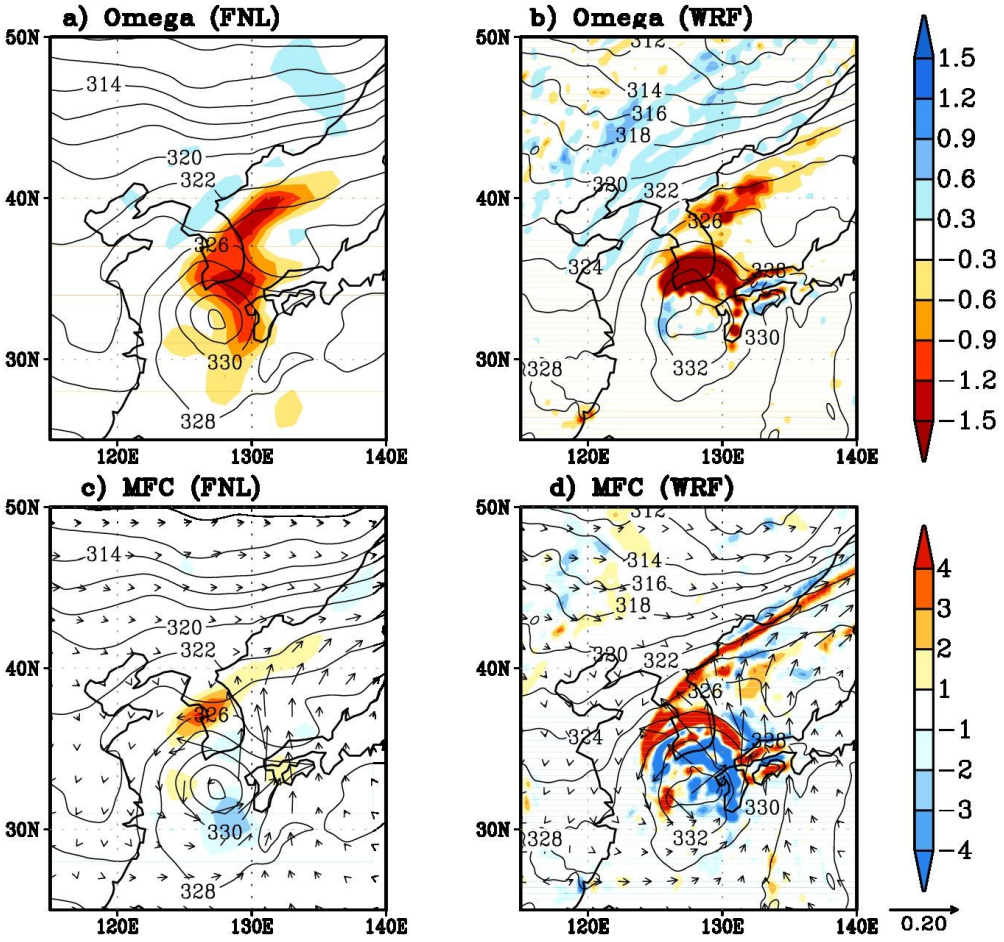

Fig. 3-7. (a, b) Pressure velocity (Pa s^{-1}) and (c, d) moisture flux (m s^{-1}, vector), moisture flux convergence (10^{-7} s^{-1}, shaded) with potential temperature (K, contour) at 500 hPa at 00 UTC 31 from the NCEP FNL data and at 23 UTC August 2002 from the outputs of the WRF/ARW model, respectively.

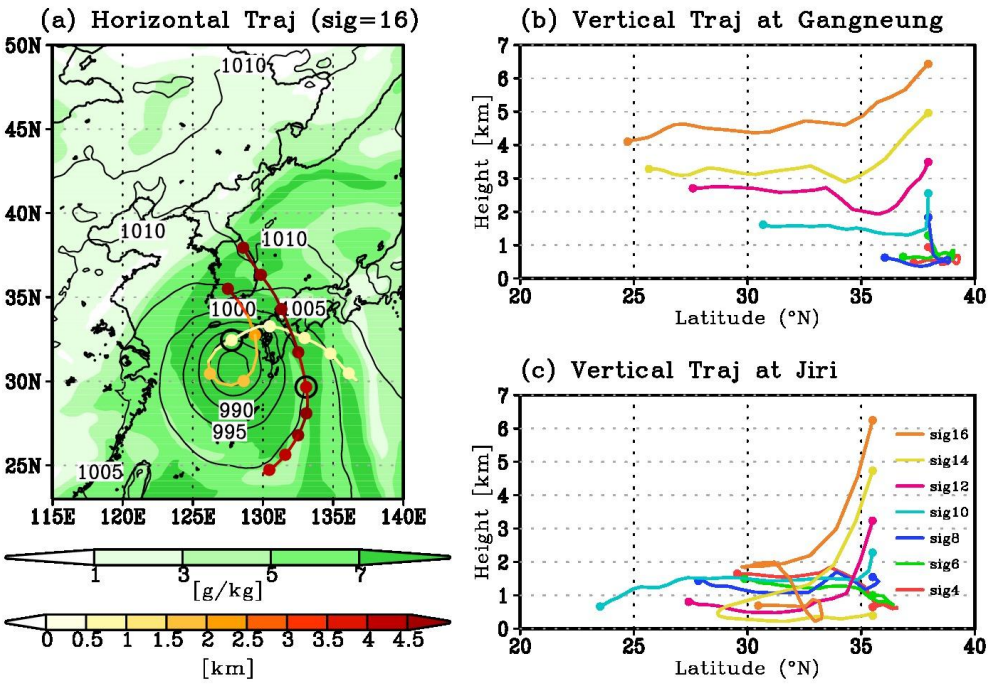

Fig. 3-8. (a) The simulated 24-hr backward trajectories started from the 0.517 sigma level of the point of maximum total precipitation and Jiri-mountain area at 23 UTC 30 August. Air parcel positions are marked every 6-hr and colored according to the height of the air parcel (km). The contour and shading denote the sea level pressure (hPa) and vapor mixing ration (g kg^{-1}) at 11 UTC 30 August, respectively. The respective air parcel positions at the time are marked by open circles. (b, c) Vertical-meridional backward trajectories from the different sigma levels at (b) the point of maximum total precipitation and (c) Jiri-mountain area, respectively.

3.2.3. Midtropospheric frontogenesis

The temporal evolution of the horizontal frontogenesis may illustrate how the front was formed ahead of the TC at the mid-troposphere (Fig. 3-9). From 12 UTC to 23 UTC 30 August (Figs. 9a and 9b), the AMF was induced by the confrontation of the TC with the midlatitude trough near the peak time of the first rainfall event in Gangneung. After the first rainfall peak, another frontogenesis occurred in the northern outer circle of the TC to the south of the AMF (Fig. 3-9c). It intensified as the TC moved northward and combined with the AMF while the TC was beginning to transform to an extratropical cyclone after 12 UTC 31 August (not shown). The latter frontogenesis at the northeast quadrant of the TC corresponds to the ET process (Harr and Elsberry 2000; Sinclair 2002). Hereafter, it is denoted as the ET-induced frontogenesis (ETF).

The total forcing of F_H and its individual forcing terms (i.e., HDF, DF, and TF as defined in Eq. (5)) were computed at 500 hPa to show the budget of the AMF (Fig. 3-10). The HDF had magnitude comparable to that of the total forcing over the frontal region, which had a maximum value of about 4×10^{-9} K m^{-1} s^{-1} (Fig. 3-10b). The HDF was generated by confluent and deformed flows between the warm southerlies related to the TC and the cold northwesterlies related to the midlatitude trough. The air flow stretched from southwest to northeast on the leeside of the trough. The axis of dilatation was aligned more parallel to the isentropes with an angle of less than 45°, which is a deformation pattern related to warm frontogenesis when a cyclonic vortex is

placed in a baroclinic zone (Keyser et al. 1988). The concentrated region with frontogenesis by the DF and frontolysis by the TF had a maximum value of about 9×10^{-9} K m^{-1} s^{-1} (Figs. 3-10c and 3-10d). The ascending motion on the warm side of the frontal region led to frontogenesis by the DF due to the release of latent heat resulted from the condensation of moist air. By contrast, the TF was associated with frontolysis because both the strong ascent on the warm side and the weak descent on the cold side across the frontal region kinematically reduced the horizontal temperature gradient. These indicate that the DF tended to counteract the TF. Although the DF and TF are larger than the HDF by the factor of 2, their patterns almost offset each other over the saturated ascent region, which was discussed in many previous researches (e.g., Ballentine 1980; Orlanski et al. 1985; Koch et al. 1995; Bryan and Fritsch 2000; Locatelli et al. 2002; Novak et al. 2004).

Time series of the individual forcings at 500 hPa were shown by averaging them over the box denoted in Fig. 3-10a (Fig. 3-11). In the time series, we can also confirm the distinction of the AMF from the ETF. The total forcing began to increase at 18 UTC 30 August, reaching a maximum at 23 UTC 30 August at the peak of the first rainfall event (i.e., the AMF). Afterwards, the front dissipated slightly from 00 UTC to 03 UTC 31 August, which coincided with the weakening of the first rainfall event. This was followed by the second intensification in parallel with the development of the second rainfall event from 03 UTC 31 August (i.e., the development of the ETF after the TC landfall). The HDF (blue solid line) contributed positively to the frontogenesis of both rainfall events while the combined forcing of the TF and DF scarcely

contributed to the frontogenesis until 09 UTC 31 August, because they offset each other. After 11 UTC 31 August, the front began to dissipate (i.e., frontolysis), because the combined TF and DF forcing presented the frontolysis, which indicates the arrival of an unsaturated region.

To show the distinctive features between the AMF and the ETF more clearly, time series of the frontogenesis function is again depicted but with the vertical distribution in the troposphere (Fig. 3-12). The AMF only occurred at the mid-troposphere during the first rainfall event, while the following ETF had a deeper vertical structure extending near the surface. Both the AMF and the ETF looked to propagate downward with time, which implies their northwestward tilted structures with height. According to Klein et al. (2000)'s definition, the transformation and reintensification stages of Rusa respectively began around 06 UTC 31 August and at 00 UTC 2 September, indicating that the AMF occurred prior to the ET process. Meanwhile, we may find the reason why the simulated hourly precipitation averaged over the frontal region was slightly divided into two during the second rainfall event (Figs. 3-6c and 3-11). The ETF generated strongly from the upper-level slightly weakened around 09 UTC 31 August, and then reintensified at the low-level. The time series of the vertical averaged ETF shows the separate peaks during the second rainfall event (not shown).

Fig. 3-12 also shows distinguishable upward motions at the low- and mid-level during the first rainfall event. Near the surface, the upward motion abidingly occurred throughout the event, which is attributed to the orographic forcing. At the mid-troposphere, upward (downward) motion occurred above (beneath) the front. This

indicates that the AMF derived the midtropospheric flows. Besides, the southerlies were intensified at the upper level during the first rainfall event (the thick solid line in Fig. 3-12), indicating the induction of the secondary circulation by the AMF. Fig. 3-13 clearly shows a prominent thermally direct (i.e., secondary) circulation cell (arrows) related to the AMF at the middle-to-upper troposphere as well as the mountain wave-like pattern at the low-level at the first rainfall peak time. The ascent on the warm side of the AMF resulted in wide spread saturation above the maximum precipitation point with relatively high hydrometeor contents on the warm side of the front that was distinctive from the low-level saturation. The southeasterlies on the upper branch of the circulation intensified the jet as described in Fig. 3-4. Consequently, the thermally direct circulation across the AMF induced the ascent at the mid-level, which could enhance the precipitation during the first rainfall event together with the orographically forced convection at the low-level.

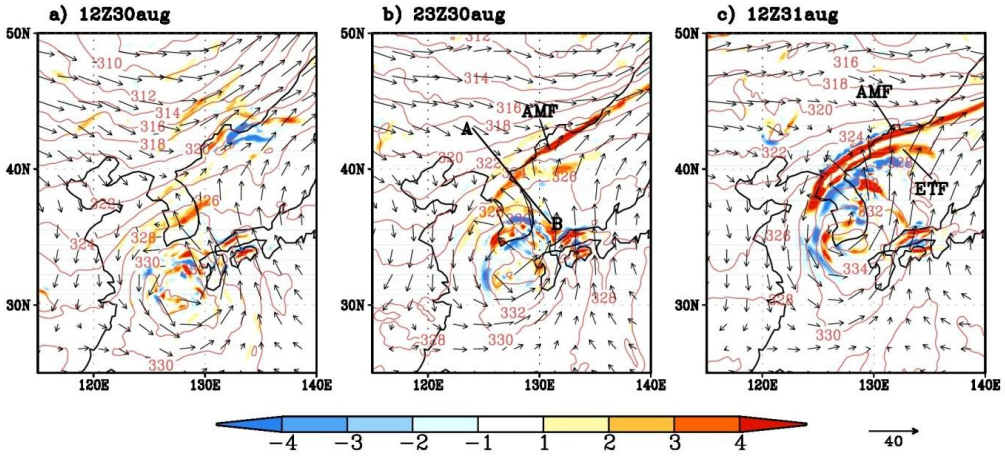

Fig. 3-9. (a) The total frontogenesis function (F_H) (1×10^{-9} K m^{-1} s^{-1}, shaded), potential temperature (K, red thin line) and horizontal winds (m s^{-1}, arrows) at 500 hPa from the outputs of the WRF/ARW model. (b) and (c) as in (a) but for 23 UTC 30 and 12 UTC 31 August, respectively. The black thick line (A–B) in (b) indicates cross-frontal direction along which the vertical cross-sections in Fig. 3-14 are plotted.

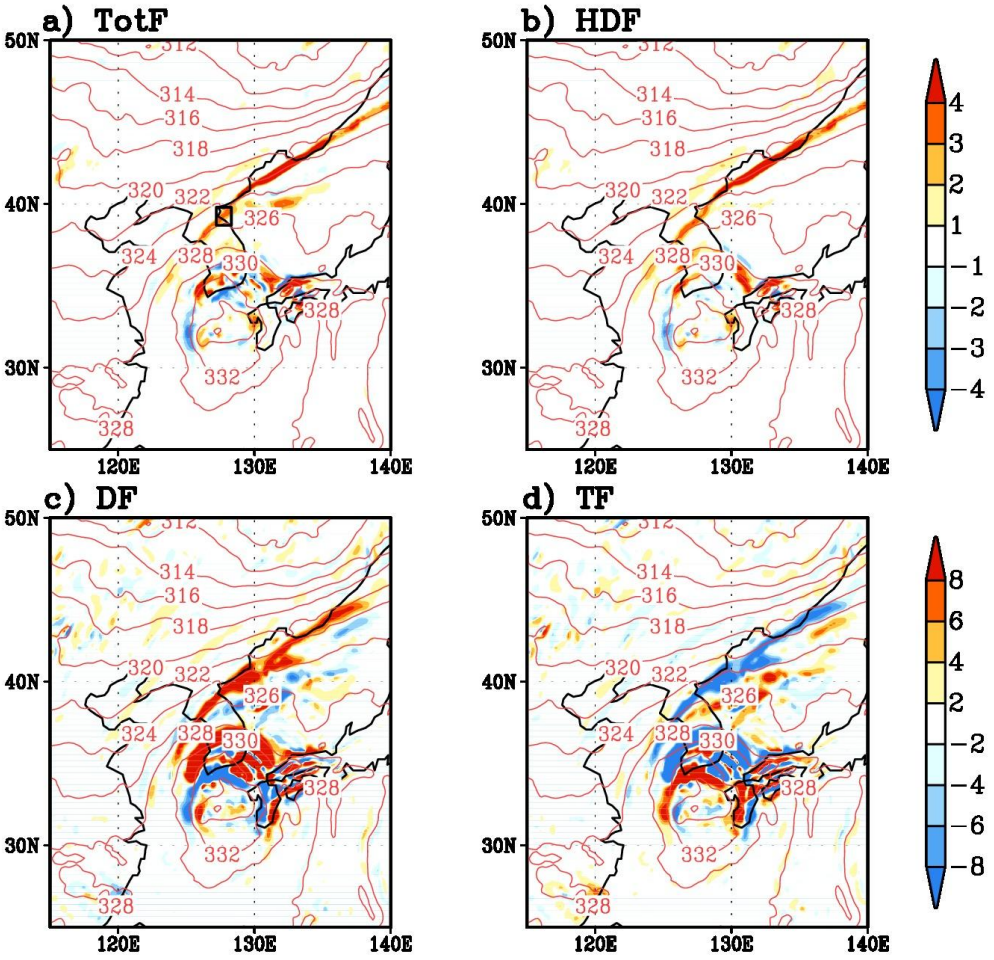

Fig. 3-10. (a) The total frontogenesis function, (b) horizontal deformation forcing, (c)diabatic forcing, and (d) titling forcing (1×10^{-9} K m^{-1} s^{-1}, shaded) with potential temperature (K, contour) at 500 hPa at 23 UTC 30 August 2002 from the outputs of the WRF/ARW model. Shadings in the top and bottom panels are at intervals of 1×10^{-9} and 2×10^{-9} K m^{-1} s^{-1}, respectively. The black box in (a) denotes the selected frontal region used to calculate the time series in Figs. 3-12 and 3-13.

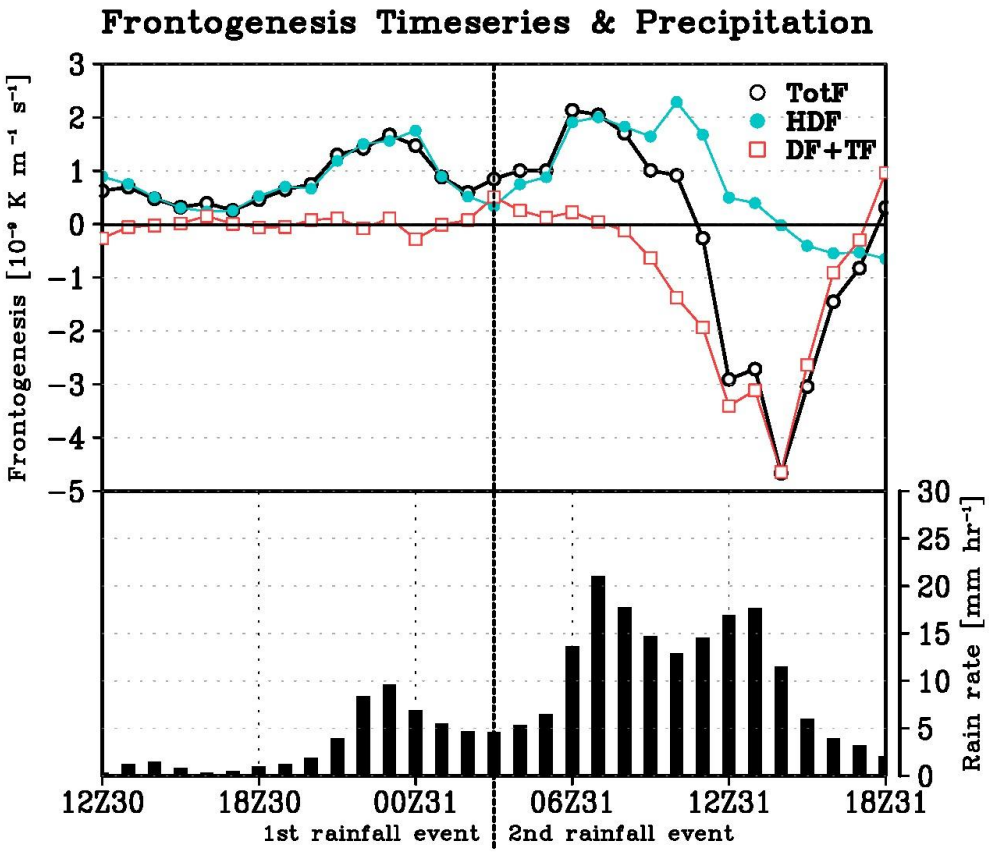

Fig. 3-11. Time series of the total frontogenesis function (black line), horizontal deformation forcing (blue line), and the sum of the diabatic and tilting forcings (red line) (1×10^{-9} K m^{-1} s^{-1}), averaged over the selected frontal region (the box in Fig. 3-11a), from 12 UTC 30 to 18 UTC 31 August 2002. The black bars at bottom represent the simulated hourly precipitation averaged over the frontal precipitation region (boxes in Fig. 3-7b).

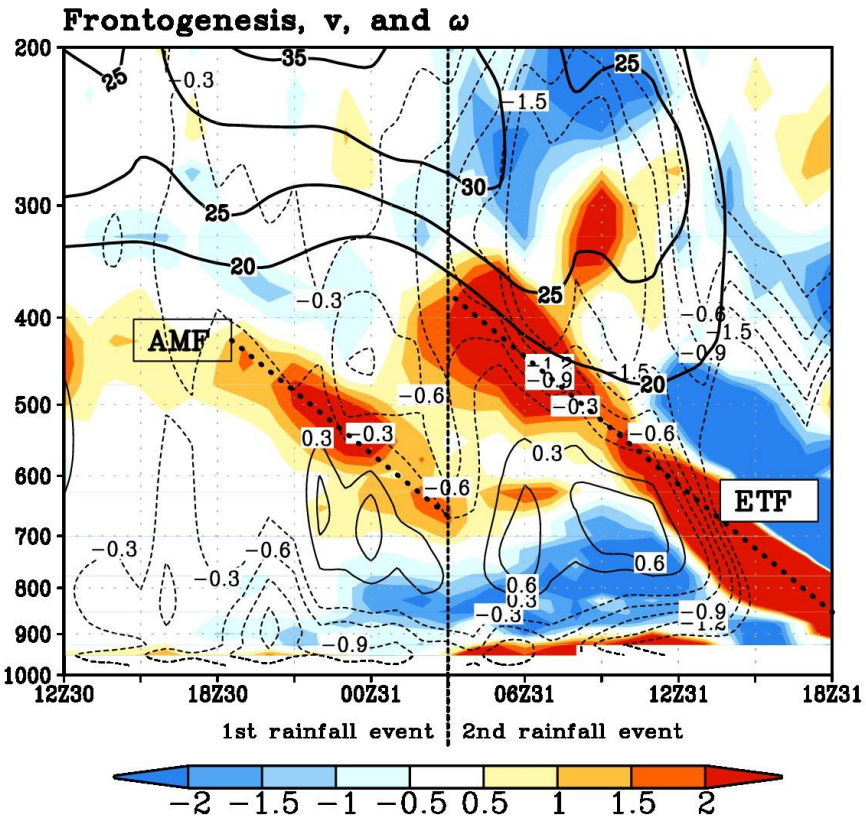

Fig. 3-12. Time series of the vertical distribution of the total frontogenesis forcing (1 × 10^{-9} K m^{-1} s^{-1}, shaded), meridional wind velocity (m s^{-1}, thick solid contour), pressure velocity (Pa s^{-1}, thin solid contour) averaged over the selected frontal region (the box in Fig. 3-12a), from 12 UTC 30 to 18 UTC 31 August 2002. Thick dotted lines denote the propagating directions of the AMF and the ETF.

3.2.4 Contribution of AMF to the AIP

The distinctive ascent and hydrometeor contents at the middle-to-upper troposphere (Figs. 3-12 and 3-13) lead us to suppose that the saturation associated with the AMF could be distinctive from that at the low-level. This supposition is in line with the interpretation from the vertical sounding (Fig. 3-5). How much does the midtropospheric saturation induced by the AMF contribute to the first rainfall event in Gangneung? From the model output, this could be quantified by the following way. The mass-weighted vertical integration of the total sedimentation of hydrometeor contents (SHC) was computed by the continuity equations for the water vapor and hydrometeor contents as described in Appendix A (Fig. 3-14). Respective integrations in the lower- (1000 to 600 hPa) and upper-layer (600 to 100 hPa) were also shown in order to estimate the individual contributions of the SHC in the lower- and upper-layer to the precipitation. Because the SHC indicates the fallout residuals after the phase exchange of water in a specific volume, the mass-weighted vertical integration of the upper- (lower-) layer represents the approximate contribution of the AMF (orographical forcing) to the precipitation. The time series of the SHC fairly coincides with that of the hourly precipitation. For example, the SHC shows a peak 1 hr before the peak of hourly precipitation during the first rainfall period. The vertically integrated SHC in the upper-layer also increases gradually in addition to the increase in the lower-layer. The amounts of the integrated SHC for the upper- and lower-layer are about 3.9 and 4.5 mm hr−1 at the peak time, respectively. This means that the contribution of the upper-layer SHC is about 46% of the total precipitation amount in

the model simulation. These simulated features suggest that the midtropospheric front might substantially contribute to the first rainfall peak, together with the orographic lifting effect.

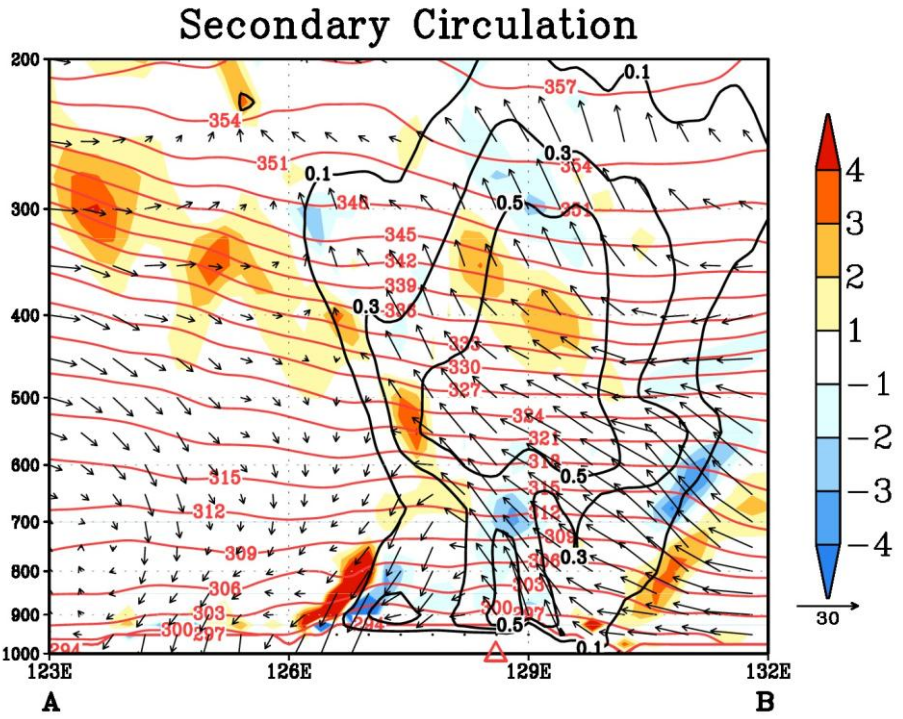

Fig. 3-13. Vertical cross-section of the total frontogenesis function (1×10^{-9} K m^{-1} s^{-1}, shaded), potential temperature (K, red contour), and wind vectors (horizontal wind (m s^{-1}) and vertical pressure velocity (10 Pa s^{-1})) at 23 UTC 30 August 2002 along the cross-frontal direction (A–B in Fig. 3-10b). The black contour denotes the sum of hydrometeor contents (kg m^{-2}). Red triangle indicates the maximum precipitation region (marked in Fig. 3-7b).

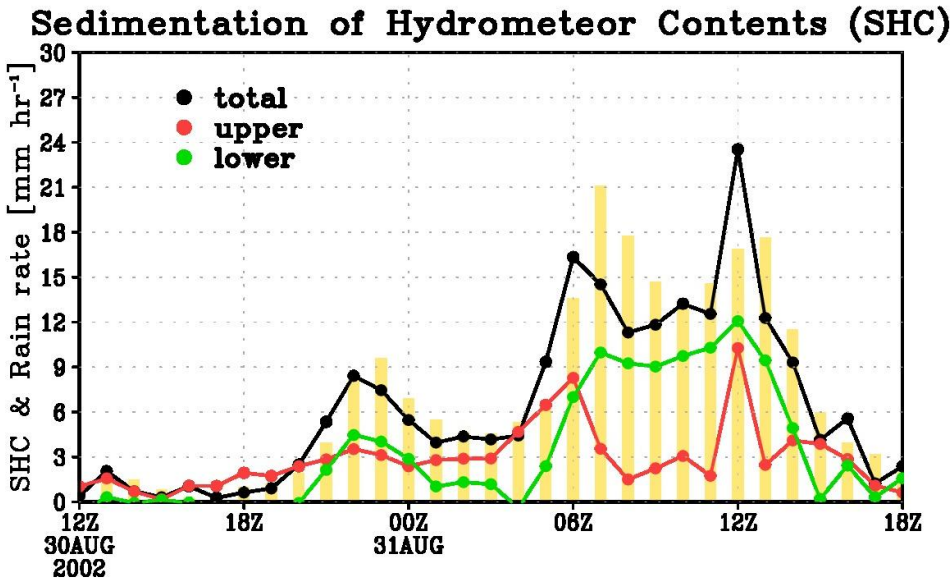

Fig. 3-14. Time series of sedimentation of hydrometeor contents (mm hr^{-1}, SHC) averaged over the frontal precipitation region (boxes in Fig. 3-7b) for the entire troposphere (black line, 1000hPa–100hPa), low-troposphere (green line, 1000hPa–600hPa), and middle-to-upper troposphere (red line, 600hPa–100hPa). The yellow bars indicate the simulated rain rate (mm hr^{-1}) averaged over the same region.

4. Comparison Study of Two Cases

This study will compare the synoptic background conditions between two representative cases with and without AIP over the peninsula. Typhoon Rammasun (2002) and Typhoon Maemi (2003) are selected for the two cases. Although both had similar tracks, made landfall, and induced heavy rainfall in the peninsula with a very similar spatial pattern of total accumulated rainfall, the temporal evolution of the induced rainfall were quite different. That is, the AIP was not observed during the approach of Rammasun, whereas it was recorded prior to the arrival of Maemi. Comparison of these cases with and without indirect precipitation can address: (*i*) the synoptic background condition favorable for the indirect precipitation prior to the arrival of TC; and (*ii*) the key physical processes responsible for the AIP.

4.1 Case Analysis

4.1.1. Track, intensity, and size

The tracks of the two TCs striking the Korean Peninsula are shown in Fig. 4-1. Typhoon Rammasun (2002) developed into a tropical storm at the northwest of Yap Island on 29 June 2002. The storm moved northwestward and gained typhoon intensity on 1 July. Rammasun weakened into a tropical storm while it accelerated northeastward after traversing near the latitude of 32°N, and then it made landfall to the west coast of the peninsula on 6 July. On the other hand, Typhoon Maemi (2003)

developed into a tropical storm northwest of Guam on 6 September 2003. Maemi moved northwestward and achieved typhoon intensity on 9 September south of the Okinawa Archipelago. After abruptly turning to the north–northeastward at 25°N east of Taiwan on 11 September, it quickly traversed the East China Sea and finally struck the south coast of Korea during the night of 12 September.

Although both TCs made landfall in South Korea, they were different in terms of intensity and size. Rammasun was weaker than Maemi (e.g., the maximum wind speeds of Rammasun and Maemi reported by the RSMC were about 44 and 54 m s−1, respectively). The intensity of Rammasun decreased after recurving and was a tropical storm at landfall. In contrast, Maemi did not quickly weaken even after recurving and struck the south coast of the Peninsula with typhoon intensity. The estimated Rammasun maximum radius of 30 knots wind or greater was 400 n mi (nautical miles) as compared to 300 n mi for Maemi.

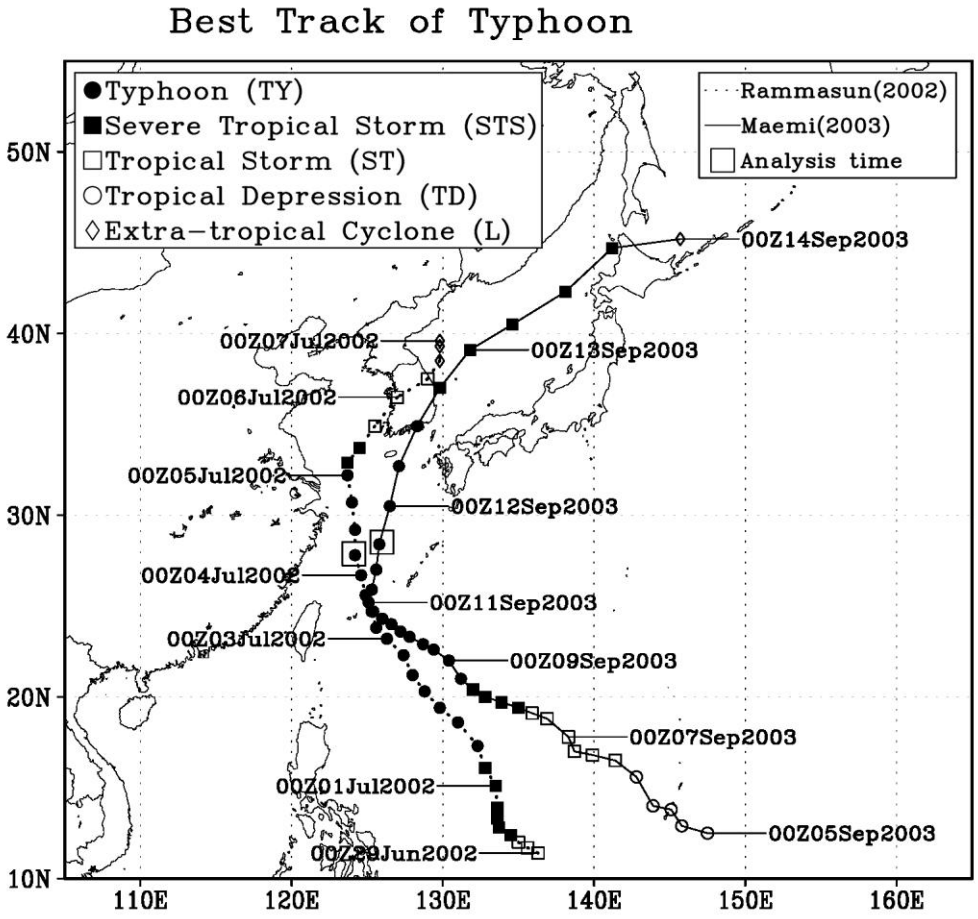

Fig. 4-1. Track and intensity of Typhoon Rammasun (2002) (dotted line) and Typhoon Maemi (2003) (solid line). The central positions are marked every six hours. The two black boxes denote the center positions of the two TCs at their respective analysis times.

4.1.2. Precipitation

The two TCs produced heavy rainfall events over the Korean Peninsula as indicated in the spatial distribution of 48-hr accumulated rainfall from gauge data in South Korea for Rammasun (Fig. 4-2a) and Maemi (Fig. 4-2b). In spite of the differences in incoming direction, intensity, and size of the two TCs, the spatial distributions are quite similar for the two. The east and south provinces experienced heavy rainfall during the approach of the two TCs. These provinces are located adjacent to steep mountains exceeding 1000 m (i.e., Taebaek Mountain Range and Jiri Mountains), which indicates the role of terrain-induced lifting effect in both cases. The accumulated rainfall amounts recorded around the Jiri Mountains (marked by a black box in Fig. 4-2) exceeded 250 mm day−1 for Rammasun and 400 mm day−1 for Maemi.

However the temporal structures of these events in the indicated box in Figs. 4-2c, d were quite different. While just one rainfall peak was associated with Rammasun (Fig. 4-2c), the rainfall evolution shows double peaks in the course of Maemi's approach (Fig. 4-2d). The heavy rainfall event associated with Rammasun and that around the second peak for Maemi can be regarded as the rainfall directly caused by strong convection in the northeast quadrant of each TC, considering their path and size at that time. However, the first heavy rainfall peak for the Maemi case occurred about 30 hours before Maemi made landfall, which is clearly outside of the direct influence of the Maemi's center convection.

The rainfall analyses from TRMM 3B42 V6 are displayed in Fig. 4-3 for the two TC cases. The analysis time for Maemi is 1800 UTC 11 September 2003, which is the nearest available time in the FNL/NCEP GFS data around the first peak. For Rammasun, the analysis time is 0600 UTC on 4 July 2002 which is when the location of Rammasun is the closest to the location of Maemi at its analysis time (see Fig. 4-1). Selecting nearby locations is expected to provide a fair comparison between the two TC cases. At the analysis time for Rammasun, the intensity of rain rate was generally smaller than 5 mm near the inner core, but a crescent-shaped intense rainband was on the northeast periphery of the TC. A weak precursory rain event ahead of Rammasun prior to 0000 UTC 5 July (Fig. 4-2c) was related to the crescent-shaped rainband. The rainband is likely to be the direct precipitation of the TC, considering the relatively large estimated size of Rammasun (dotted black circle in Fig. 4-3a). For the Maemi case, two distinctive rainbands were observed. One was present near the inner core of the TC, and the other was over South Korea. The latter precipitation feature was situated well outside the effective size of Maemi (Fig. 4-3b), so it can be classified as an AIP.

The satellite imagery in Figs. 4-3c, d shows the distributions of cloud shields related to convection and precipitation. The IR images clearly illustrate the distinctive synoptic regimes over East Asia between the two events. In the Maemi case, shading in the clear areas over land is slightly lighter than that in the Rammasun case, which indicates that the land surface was cooler in the Maemi case to the northwest of the peninsula. This reveals that the stronger background baroclinicity in the Maemi case,

compared with the Rammasun case. As a result of low baroclinicity, precipitation was not recorded over the peninsula at the analysis time of Rammasun, even though the high cloud zones extended toward the peninsula. Thus the cloud shield over the Peninsula was not the convective type inducing precipitation. For the Maemi case, a thick cloud shield existed around the TC and an elongated cloud band extended from the TC northeastward toward the midlatitudes to form a number '6' shape (Fig. 4-3d). This elongated cloud band was collocated with the separate intense precipitation over the peninsula, which indicates that first rainfall event of Maemi case was related to front-type convective band.

If two ideal TCs with identical properties except for their size enter the same midlatitude baroclinic environment, it would be natural to assume that the larger one would interact with the midlatitude environment more effectively. However, the small-sized Maemi seemed to more vigorously interact with the midlatitude baroclinic environment than Rammasun in the sense that the intense AIP was induced by the interaction of Maemi with the midlatitude environment. Accordingly, it can be inferred that different synoptic background conditions interacted with the two TCs. We will discuss the differences in terms of synoptic background conditions and propose a possible mechanism for the AIP next.

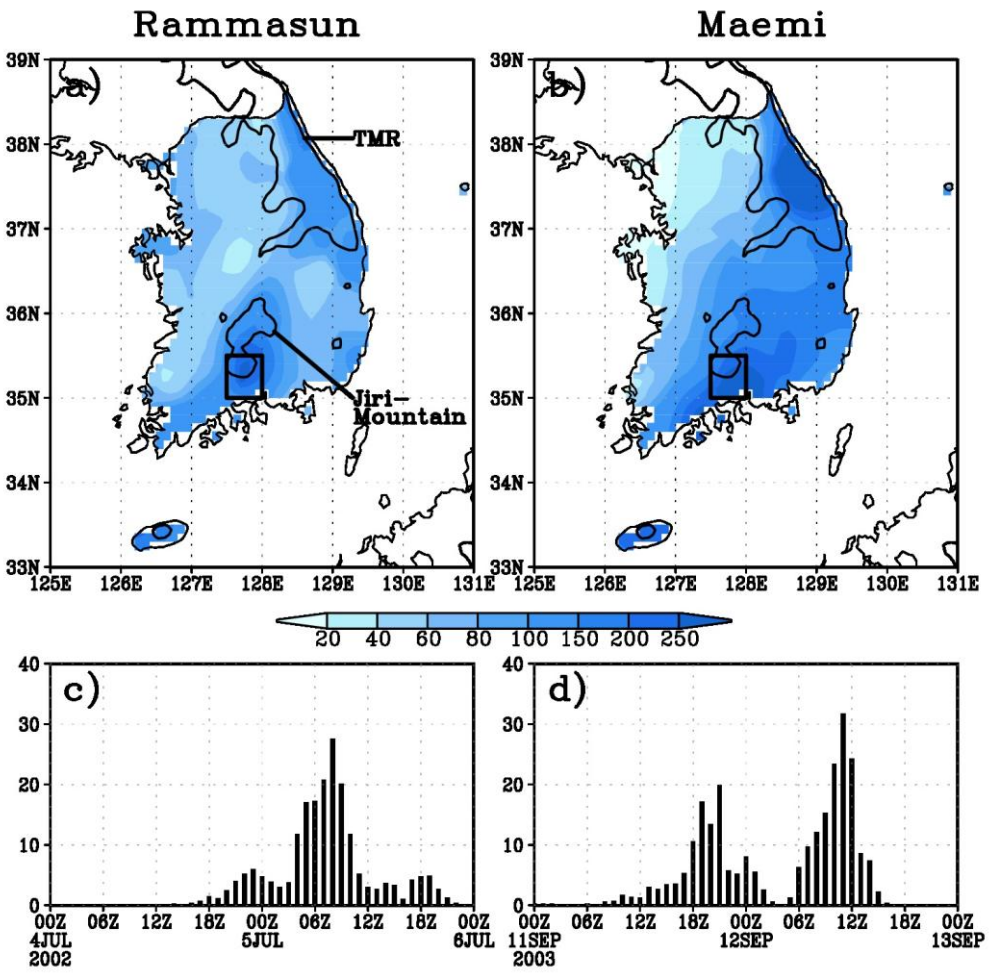

Fig. 4-2. Accumulated precipitation (mm 48-hr^{-1}; shading in (a, b)) and time series of hourly precipitation averaged in the black box (c, d) from gauge data in South Korea for Rammasun (left panels) and Maemi (right panels). The contours in (a, b) denote the mountain areas with a terrain height over 450 m.

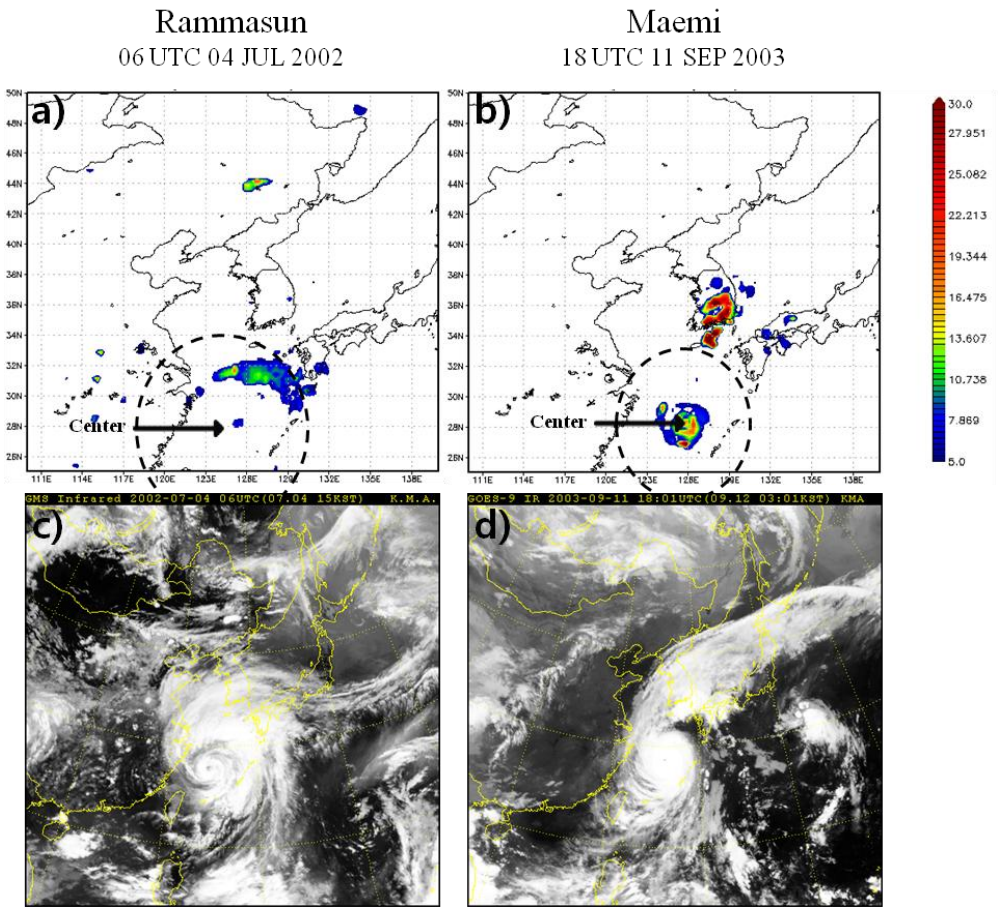

Fig. 4-3. 3-hr accumulated rain rates (mm hr^{-1}) from the TRMM 3B42 V6 data (a, b) and enhanced IR images from the GMS (c, d) for Rammasun (left panels) and Maemi (right panels) at their respective analysis times in Fig. 4-1. Dashed circles in panels (a) and (b) indicate the approximate maximum radius of 15 m s^{-1} wind or greater of the two TCs estimated by the RSMC Tokyo – Typhoon Center.

4.2 Possible mechanisms for differences of two cases

A possible mechanism that leads to the AIP ahead of a TC is examined via a comparison of Maemi with Rammasun at their respective analysis times (i.e., Rammasun: 0600 UTC 4 July 2002; Maemi: 1800 UTC 11 September 2003). Based on the differences in the precipitation and cloud shield patterns between the two TCs, it is inferred that the AIP associated with Maemi occurred due to the difference in the TC–environment interaction. Thus, the synoptic background associated with the AIP is described in Section 4a, the TC–environment interaction that forms the frontal features is presented in Section 4b, the source of moisture that is critical for the AIP is identified in Section 4c, and the cross-frontal secondary circulation is discussed in Section 4d.

4.2.1. Synoptic background

Analyses of the synoptic environment at 200, 500, and 850 hPa are shown in Fig. 4-4 at the respective analysis times of the two TCs when both TCs were located about 700 km from the south coast of the Korean Peninsula. Rammasun was to the south of the upper-level ridge over the peninsula and to the southeast of the upper-level trough over East China (Figs. 4-4a, c). By contrast, Maemi was to the east of a deep upper-level trough over China (Figs. 4-4b, d). In both cases, an upper-level trough was seen over mainland China, which contributes to the recurvature of the TCs. Notice that Maemi recurved more sharply (Fig. 4-1) because of the stronger trough for the Maemi

case. The key differences, however, lie farther northeast in the structure of the upper-level flow. In the Rammasun case, there was a split flow pattern east of the trough over East China, with a deep low over northeast of the peninsula and a trough east of Japan (Figs. 4-4a, c). The shearing deformation between the trough over East China and the low northeast of Korea allows the subtropical ridge over Japan to extend northwestward over the peninsula (Fig. 4-4c).

In contrast, a strong zonal midlatitude flow was apparent north of 40°N for the Maemi case (Figs. 4-4b, d). The deep trough over the Sea of Okhotsk and ridge over Japan resulted in a strong westerly jet northeast of the Korean Peninsula. Moreover, the confluent flow between the midlatitude westerlies and the southeasterlies from the trough over East China also enhanced the westerly jet. Thus, the equatorward jet entrance region over the peninsula, and it produced a deep southwesterly flow which mitigated the northwestward progression of the subtropical high seen in the Rammasun case. The mid-level flow pattern to the north of Maemi established a strong horizontal confluent deformation field over the central Peninsula (Fig. 4-4d). The confluent deformation field formed enhanced temperature gradients (i.e., a frontal structure) as the warm and moist air from the TC met the cold and dry air from the midlatitude trough. As a result, stronger baroclinicity facilitated synoptic-scale ascent which could organize convection that produced the AMF.

At 850 hPa, the southerly flow on the right side of Rammasun did not extend to the peninsula as a westward extension the subtropical high was present to the north of the TC (Fig. 4-4e). The predominant high over the peninsula retarded the northward

transport of the deep tropical moisture from Rammasun. By contrast, the low-level moist air reached the southern part of the peninsula for the Maemi case (Fig. 4-4f). The effective moisture transport between the TC and the subtropical high was also a critical factor for the AIP over the peninsula.

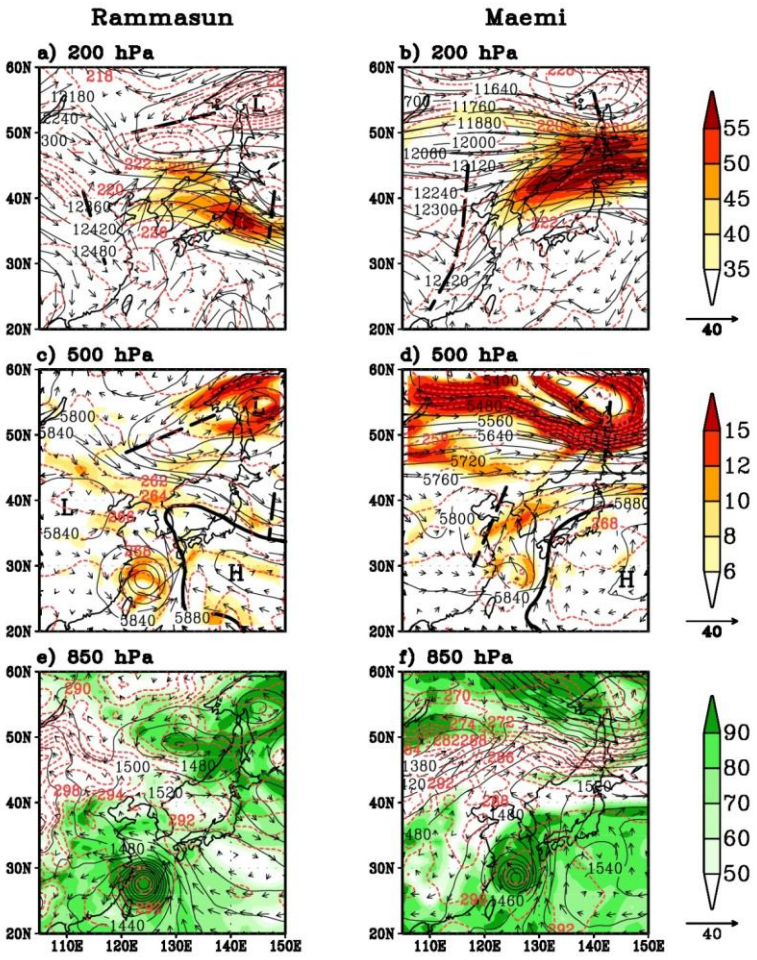

Fig. 4-4. Geopotential heights (gpm; solid contours), temperatures (K; dashed red contours), and horizontal winds (m s^{-1}; vectors) at 200 hPa (a, b), 500 hPa (c, d), and 850 hPa (e, f) for Rammasun (left panels) and Maemi (right panels) at their respective analysis times. Shadings represent 200 hPa wind speed (m s^{-1}) (a, b), (c, d) 500 hPa temperature gradient (K m^{-1}) (c, d), and 850 hPa relative humidity (%) (e, f). Thick dashed line, thick solid line, 'H', and 'L' denote the axis of trough, 5880 gpm, subtropical high, and low pressure, respectively.

4.2.2. Frontogenesis

The front-related parameters (e.g., divergence, thermal advection, and vertical pressure velocity) at 500 hPa for the two TC cases are examined to investigate how TC–midlatitude interaction leads to the strong frontogenesis over the Korean Peninsula in the Maemi case. In the Rammasun case, the annular-type convergence was found with the stronger convergent band concentrating at the northern outer cyclonic boundary where the TC was in contact with the subtropical high (Fig. 4-5a). The warm advection due to southerlies at the eastern semi-circle of Rammasun was well confined south of 33°N (Fig. 4-5c), and thus strong ascending motions occurred only within the circulation of the TC (Fig. 4-5e). In contrast, a region of strong convergence extended from the Yellow Sea through the middle of the Korean Peninsula in the Maemi case (Fig. 4-5b). Considering the effective size of Maemi (Fig. 4-3b), the convergent region therefore formed outside of the TC. Strong warm advection also occurred along a line oriented from southwest to northeast over the southern part of the peninsula (Fig. 4-5d), which did not exist in the Rammasun case. Therefore, warm and moist air was conveyed toward the peninsula in association with the strong southerlies of Maemi, and converged between the TC and midlatitude trough. These circulations generated a warm front, which was represented by a steep temperature gradient over the Peninsula (Fig. 4-4d). This frontogenesis helped ascending motions (i.e., convection) and precipitation on the warm side of the front, which intruded into the southern province of the Peninsula (Fig. 4-5f).

The distributions of front-related parameters in the Maemi case are consistent with the rainy regions in the TRMM rainfall data (Fig. 4-3b) and the satellite observed IR cloud shield images to a large extent (Fig. 4-3d). These features imply that the thermally direct circulation associated with the warm front was enhanced by the interaction of Maemi with the midlatitude trough. This is highly likely to be the cause for the intensification of the first rainfall event of Maemi (Figs. 4-2d, 4-3b).

Each of the three-dimensional horizontal frontogenesis equation (Eq. (5)) is examined to illustrate how the TC–trough interaction contributed to the frontogenesis in the Maemi case (Fig. 4-6). In the Rammasun case, none of these forcing terms had any notable magnitude over the peninsula (left panels of Fig. 4-6). In the Maemi case the contribution from the total forcing is a maximum in the southern province of the Peninsula (Fig. 4-6b).

Contributions of the individual HDF, DF, and TF terms were also clearly found in the Maemi case (Figs. 4-6d, f, h). The HDF generated by confluent flows was slightly larger than the total forcing and was nearly collocated with the frontal region (Fig. 4-6d). This HDF was generated by confluent flows in the midst of the TC, subtropical high, and midlatitude trough. The contribution to frontogenesis (frontolysis) by the DF (TF) term extended from southwest to northeast and covered the region of the total forcing. Although the magnitudes of the DF and TF terms are about 2 times larger than that of HDF (Figs. 4-6f, h vs. Fig. 4-6d), the DF and TF terms almost offset each other within the saturated ascending region. That is, the DF term counteracted against the TF term as has been found in previous studies (e.g., Ballentine, 1980; Orlanski et al.,

1985; Koch et al., 1995; Bryan and Fritsch, 2000; Locatelli et al., 2002; Novak et al., 2004). It should note that the calculation of diabatic heating from the coarse resolution of the FNL/NCEP GFS data may suffer from the reliability issue, though the method using air parcel trajectories may help mitigate this issue (Cordeira and Bosart, 2011). The ascending motion on the warm side of the frontal region contributes to frontogenesis via the DF terms due to the condensational heating of moist air (Fig. 4-6f). In contrast, the TF generally reduced the horizontal temperature gradient by inducing the strong ascent on the warm side of the frontal region that causes kinematical frontolysis (Fig. 4-6h). Therefore, we can conclude that the HDF, which was larger than the addition of TF and DF, generated the midtropospheric front, and, in turn, contributed to the AIP of Maemi.

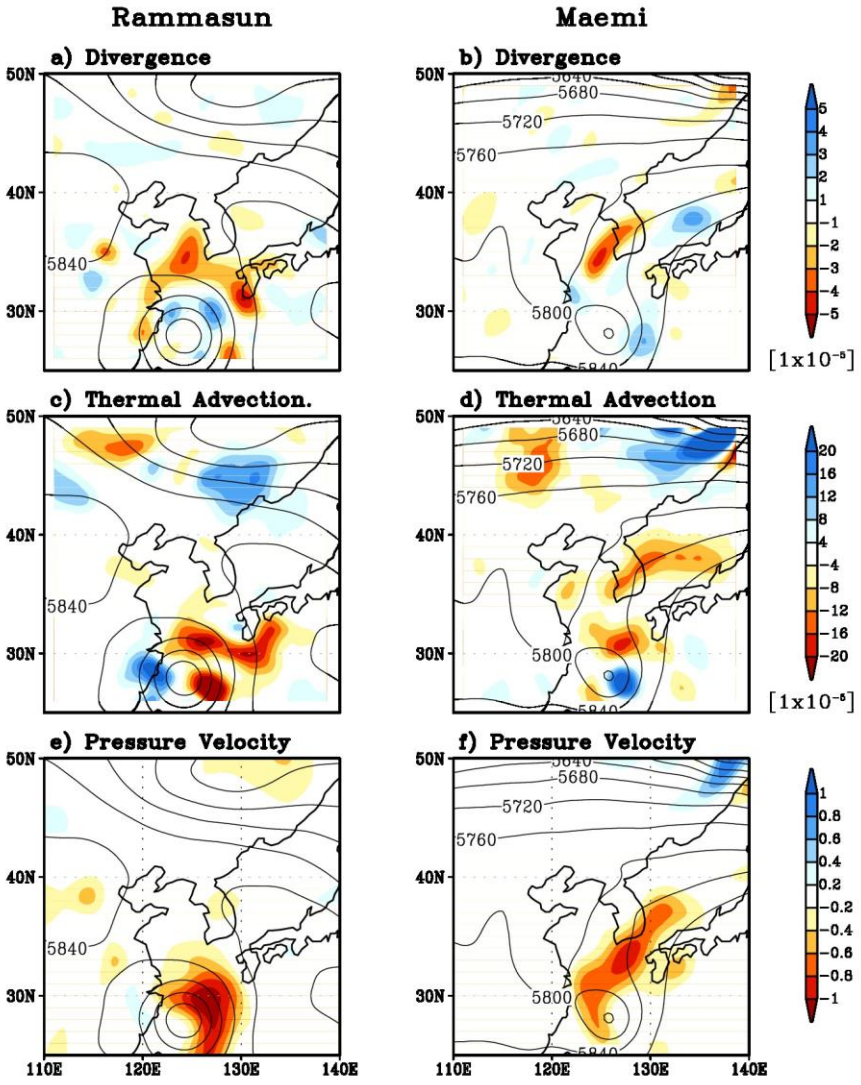

Fig. 4-5. Divergence (10^{-5} s^{-1}) (a, b), thermal advection (10^{-5} K s^{-1}) of potential temperature (c, d), and pressure velocity (Pa s^{-1}) at 500 hPa (e, f) for Rammasun (left panels) and Maemi (right panels) at their respective analysis times. Negative values in the thermal advection indicate warm advection. The contours denote the 500-hPa geopotential height (gpm).

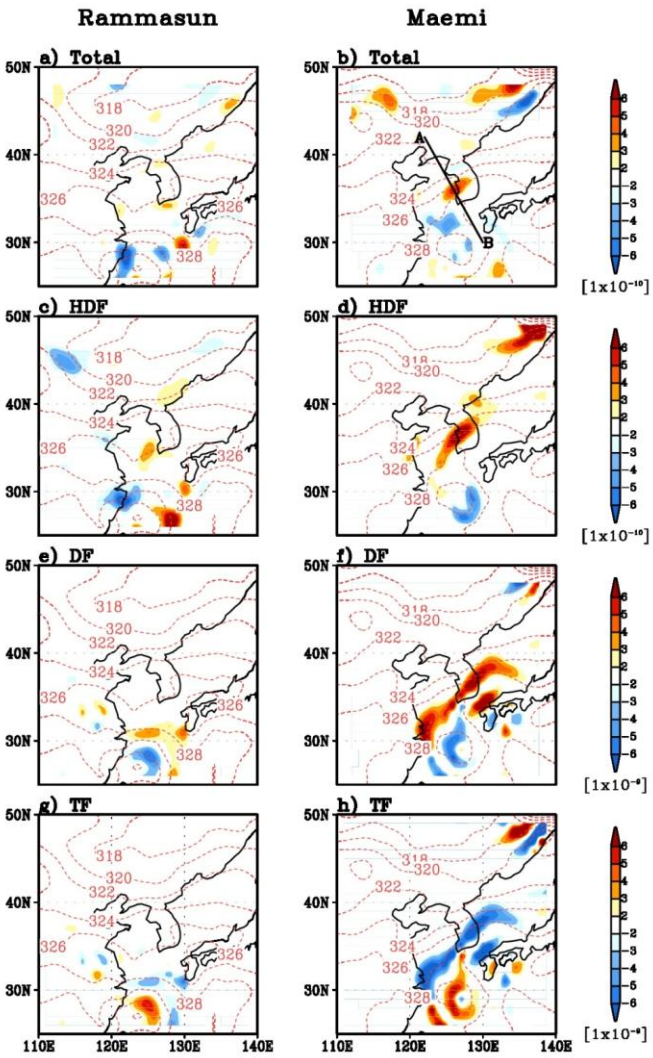

Fig. 4-6. Total frontogenesis function (F_H) (a, b), horizontal deformation forcing (HDF) (c, d), diabatic forcing (DF) (e, f), and tilting forcing (TF) (g, h) at 500 hPa for Rammasun (left panels) and Maemi (right panels) at their respective analysis times. The dashed red contours denote the 500-hPa potential temperature (K). Shading intervals in the two top panels and two bottom panels are 10^{-10} K (m s)$^{-1}$ and 10^{-9} K (m s)$^{-1}$, respectively. The line A–B is the axis of the vertical cross-section in Fig. 4-8.

4.2.3. Moisture transport

Deep moisture is a key ingredient for heavy rainfall (Doswell et al. 1996). In addition to the frontogenetical mechanism proposed in this study, abundant low-level moisture supply by the southerly wind on the east side of Maemi could contribute to the intense AIP similar to the mechanism proposed by Schumacher et al. (2011) and Wang et al. (2009) (Figs. 4-4e, f). The area with 90% relative humidity extended from Maemi to the southern province of the peninsula. For the Rammasun case, the subtropical high extended to the peninsula and blocked the northward moisture transport, resulting in a relatively dry air mass along 34N with relative humidity values < 70% (Fig. 4-4e). Here more intuitive analysis is provided in terms of the moisture transport.

Moisture flux and its convergence at the respective analysis time of the two TCs and the 36-hr trajectory (from the analysis time to 36-hr before) back-traced from the grid point at 850 hPa near Jiri Mountains (the box in Fig. 4-2) were shown in Fig. 4-7. For the Rammasun case, the moist air of the TC did not reach the peninsula, but stayed within a few hundred km from the center convection due to sustaining circular flows (Fig. 4-7a). In contrast, the area with large moisture convergence was collocated with the location experiencing heavy rainfall (Fig. 4-7b vs. Fig. 4-3b). The southwest–northeast elongated band of moisture flux convergence was associated with the rainfall over the southern part of the front. The three-dimensional 36-hr backward trajectories also clearly support the explanation. A backward trajectory (from the analysis time)

from the location of AIP indicates that the moisture source for the AIP in the Maemi case originated from the subtropical ocean surface. The air parcel was quickly advected along the eastern side of Maemi. In the Rammasun case, however, the air parcel was slowly advected from the upper-level around the Kyushu Island (Fig. 4-7a), which indicates that Rammasun's circulation was less influential on the air parcel trajectory. The intrusion of warm and moist air of Maemi could enhance convective instabilities below the AMF, and contribute to the AIP over the frontal region ahead of the approaching TC.

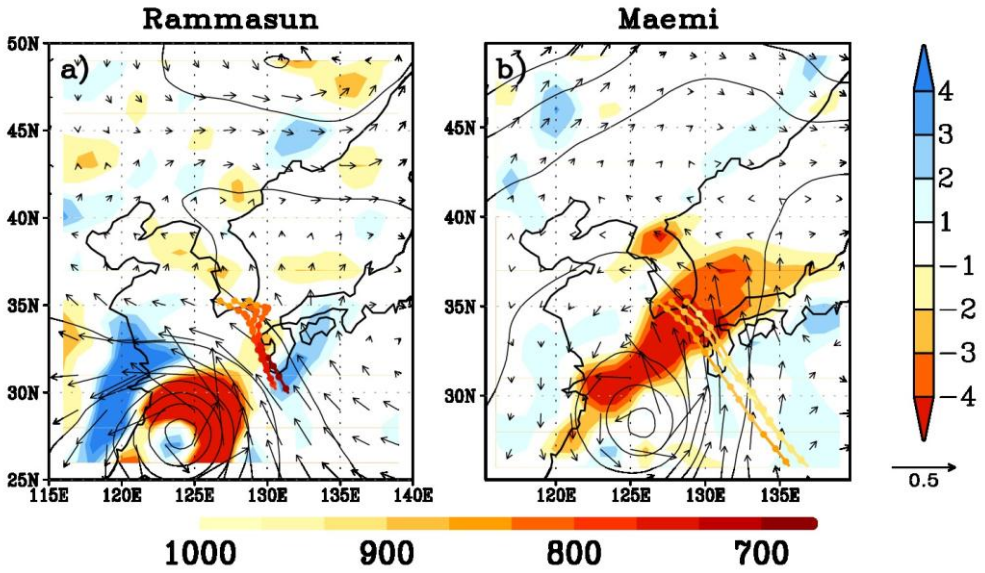

Fig. 4-7. 850-hPa moisture flux (g kg^{-1} m s^{-1}; vectors) and its divergence (g kg^{-1} s^{-1}; shadings) for Rammasun (a) and Maemi (b) at their respective analysis times. The right-side vertical color bar corresponds to the 850-hPa moisture flux divergence. The color lines are 36-hr backward 3-D air parcel trajectories at 1-hr intervals, which start from the analysis time at 850 hPa of three grid points around Jiri Mountains ((35.25°N, 126.75°E,), (35.25°N, 127.75°E), and (35.25°N, 128.75°E)). The circles are marked every three hours. The pressure levels along the trajectories (hPa) are color-shaded with its color bar at the bottom.

4.2.4. Secondary circulation

A thermally direct circulation can be expected with a positive frontogenesis function at the mid-troposphere (e.g., Martin et al., 1992). The total frontogenesis function (shading) and ageostrophic circulation (arrows) related with frontogenesis along the cross-frontal line (a black line in Fig. 4-6b) is shown in Fig. 4-8. Several frontogenesis regions are visible in the cross section, among which three are noteworthy: one in upper-level at the higher latitude, another in mid-level at 37°N, and the third in low-level at the lower latitude. The upper- and low-level frontogeneses were respectively induced by a confluent flow of upper-level trough (Fig. 4-4b) and the northern boundary of the TC circulation, respectively (Fig. 4-4f). The AMF occurred near 500 hPa where the HDF was the main forcing to generate the front. The DF and TF terms cancelled each other in a saturated environment, thus the HDF is sufficient to explain the AMF.

A typical thermally direct circulation around a central frontal region exists at mid-levels well-displaced from TC center (28°N). The slantwise ascent was very intense on the warm side of the front, while the descent on the cold side was weak. Large vertical wind shear also appeared along the front with low-level easterlies along the northern periphery of the TC below the upper-level westerlies related to the trough (see Fig. 4-4b). The vertical wind shear is dynamically consistent with a strong horizontal temperature gradient based on the thermal wind relationship. The thermally direct circulation that is intensified by the convection in the warm and moist air is thus

associated with the AIP in front of the upper-level trough.

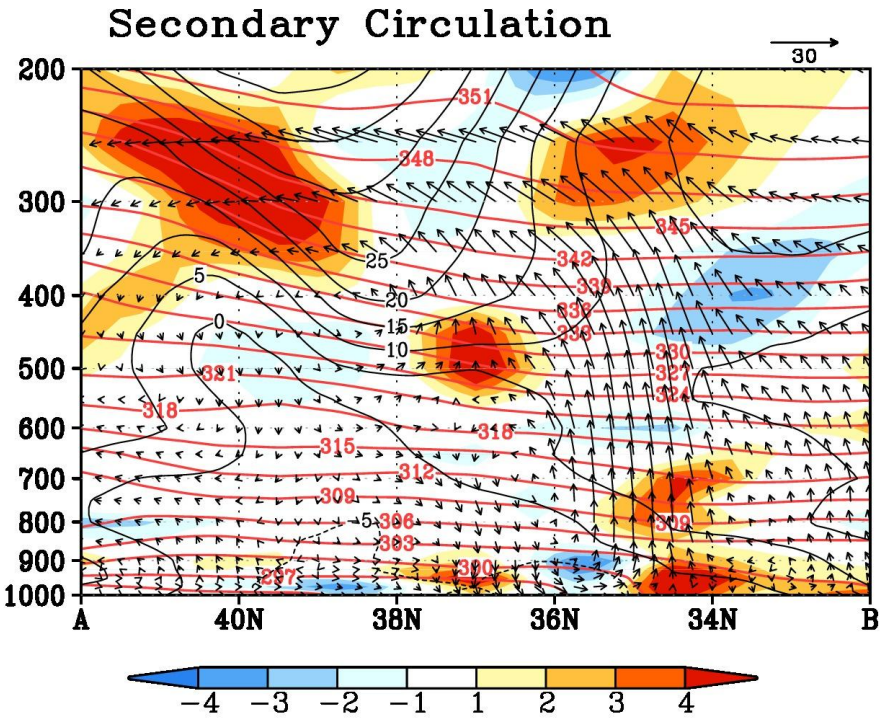

Fig. 4-8. Vertical cross-section of the total frontogenesis (10^{-10} K m^{-1} s^{-1}; shadings) and the secondary circulation (vectors) of the horizontal ageostrophic wind components (V_a) (m s^{-1}) and negative pressure velocity (30 × Pa s^{-1}) along the line A–B in Fig. 4-6b at the analysis times of the Maemi case. The black lines (short dashed for negative values) are the isotachs of along-frontal wind (m s^{-1}), and the red lines are the isotherms of potential temperature (K).

5. Statistical Analysis

In this section, we found that many cases showed double precipitation peaks, including the AIP, associated with TCs that were approaching the Korean Peninsula. Fig. 5-1 shows three examples among the AIP cases used in this study. The AIP occurred over the Korean Peninsula, showing cloud shield and precipitation distinctive from the TCs'. Considering their paths and sizes, the second peak of each case can be regarded as the rainfall directly caused by TC convection. However, the first rainfall peak occurred during antecedent time before the TC's direct rain band ever reached the Korean Peninsula. The precipitation region resided clearly outside of the effective size (defined in Section 3a) of the TC. In order to generalize the characteristics of the AIP occurrence, we collected all the TC cases that influenced the Korean Peninsula and classified them into two groups depending on the presence of AIP over the Korean Peninsula.

5.1 Statistical Properties

5.1.1. Case identification

There are no commonly accepted definitions of indirect precipitation ahead of a TC and a separation distance between the TC and the indirect precipitation region. Galarneau et al. (2010) defined the PRE based on radar image and moisture advection associated with TC. However, there is no available radar data over the ocean around

the Korean Peninsula. Byun and Lee (2012) defined the separation distance between the TC and the indirect rainfall region (i.e., critical radius) as a sum of the longest radius of 15.4 m s−1 winds, the maximum radius of the rain fields induced by the TC itself, and the 6-hourly moving distance of TC. However, their critical radius is too long to discriminate the indirect precipitation from the direct precipitation of TC; for example, Typhoon Rusa (2002) and Maemi (2003) that belong to the AIP cases with pronounced double peak patterns of hourly precipitation are falsely excluded from the AIP cases.

We suggested a practical definition of AIP in the Korea Peninsula be the precipitation recorded at the surface stations located farther than the effective radius of a TC as concerned in the case study of Typhoon Rusa (2002). The effective (or critical) radius of a TC is simply determined by the information on the longest radius of 15 m s−1 wind (R15), or greater, provided by the RSMC dataset (Fig. 5-2). We divide the 41 TC cases collected into two groups, depending on the presence of AIP over the Korean Peninsula. A TC is classified as the AIP case if the maximum 6-hr precipitation exceeding 30 mm $(6h)^{-1}$ was recorded at least by one station in South Korea during the antecedent period of the TC (i.e., defined as the period from 48 hr to 12 hr before the landfall time). Otherwise, it is classified as the non-AIP case. According to the definition, 24 cases out of the total 41 TC cases are classified as the AIP cases (Table 5-1), and the rest (17 cases) are classified as the non-AIP cases (Table 5-2). Note that the AIP cases occurred more frequently, about 58.5%, in the Korean Peninsula compared to the non-AIP cases. This fact reveals that AIP deserves to be considered as

an important factor in forecasting the precipitation associated with approaching TC over the peninsula.

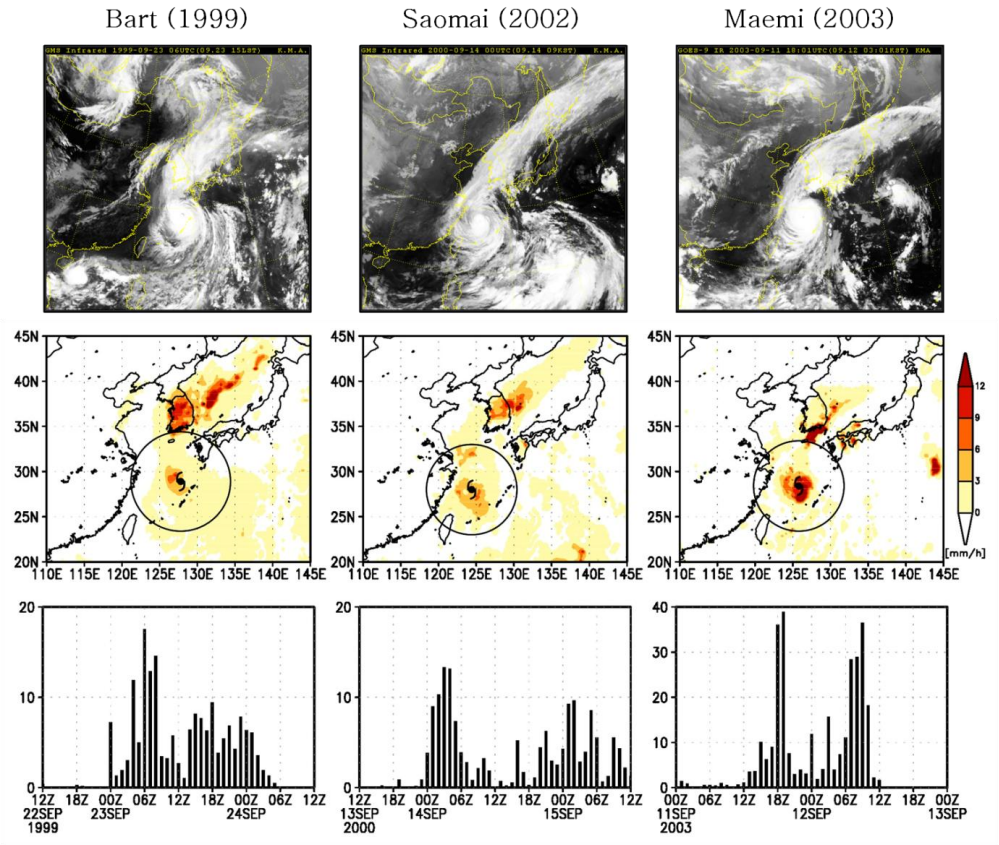

Fig. 5-1 IR images from the GMS (upper panels) and rain rates (mm hr^{-1}) from the TRMM 3B42 V6 data together with the effective radius of TC (middle panels) at the peak time of the first rainfall (see the text). The bottom panels show the time series of hourly precipitation from surface station recorded maximum precipitation in South Korea during the period associated with the TCs for the three AIP cases: Bart (1999; left), Saomai (2000; middle), and Maemi (2003; right).

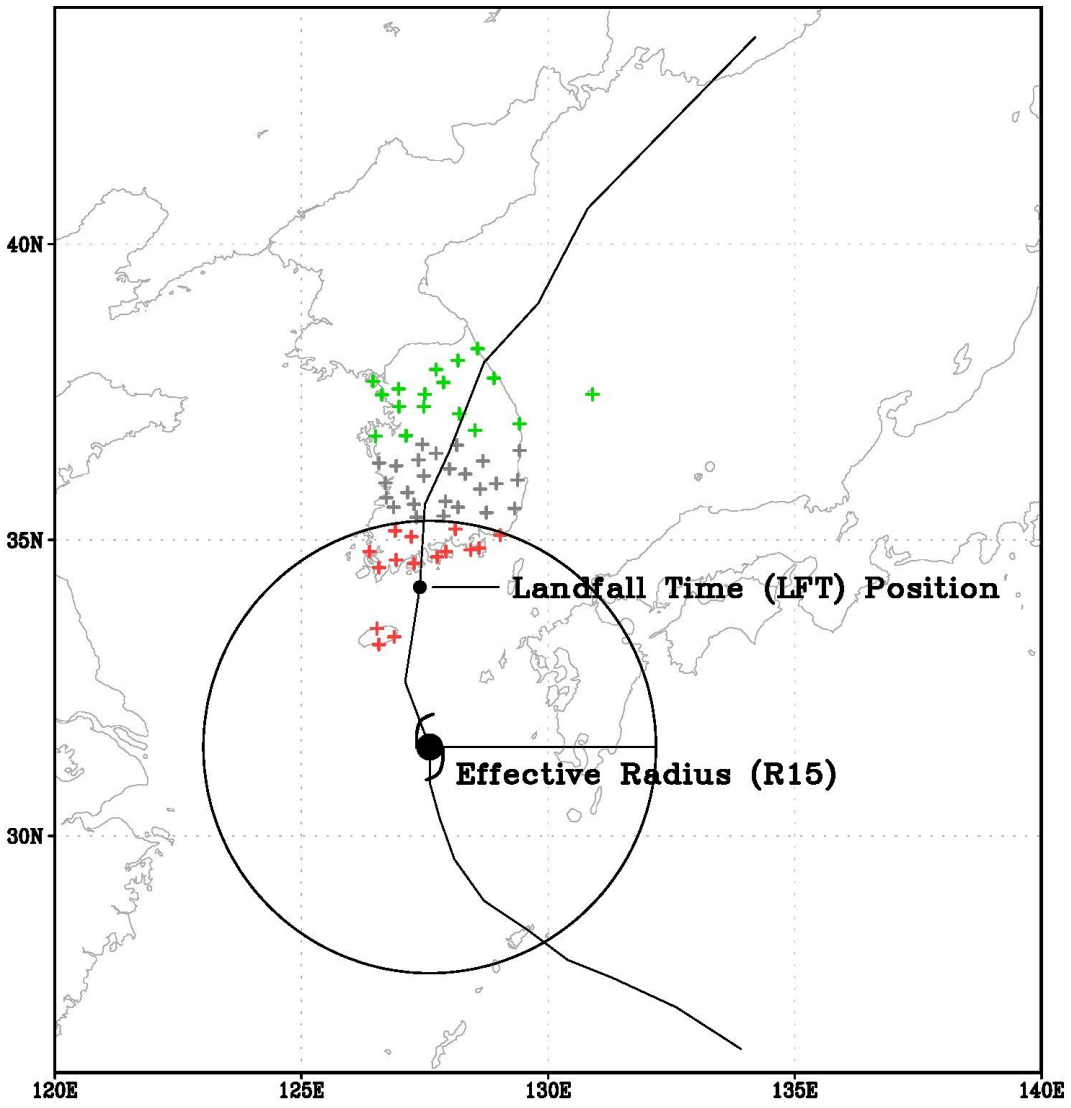

Fig. 5-2 Schematics of effective radius (R15) of TC, landfall time (LFT), and the station locations for direct (red crosses) and indirect (green crosses) precipitation. Gray crosses denote the stations that did not have precipitation. Black line denotes the TC track.

Table 5-1. List of all documented AIP cases over the Korean peninsula during 1993-2004. It contains year, parent TC of the AIP case (TC name), landfall time (LFT), analysis time (T0), maximum 6-hr precipitation at analysis time (Prep), the surface station recorded maximum precipitation (Stn), and time difference between LFT and T0 (diff).

Year	TC name	LFT	T0	Prep	Stn	diff
1993	percy	18Z29JUL	00Z29JUL	129	Suwon	18
1993	robyn	00Z10AUG	06Z08AUG	145	Jecheon	42
1993	yancy	12Z03SEP	06Z02SEP	52	Seoul	30
1994	doug	06Z11AUG	12Z10AUG	90	Sokcho	30
1995	faye	06Z23JUL	06Z22JUL	110	Jeju	24
1995	janis	12Z26AUG	18Z24AUG	265	Boryeong	42
1995	ryan	18Z23SEP	00Z23SEP	109	Sokcho	18
1996	kirk	00Z14AUG	12Z12AUG	72	Gwangju	36
1997	tina	18Z08AUG	00Z07AUG	99	Mokpo	42
1998	yanni	06Z30SEP	18Z29SEP	103	Geoje	12
1999	olga	00Z03AUG	06Z02AUG	190	Yeongju	18
1999	ann	12Z20SEP	12Z19SEP	159	Sanchoen	24
1999	bart	00Z24SEP	06Z23SEP	86	Uljin	18
2000	kai-tak	06Z11JUL	12Z10JUL	138	Haenam	18
2000	bolaven	00Z31JUL	06Z29JUL	36	Cheonan	42
2000	saomai	18Z15SEP	00Z14SEP	72	Seosan	42
2002	rusa	06Z31AUG	18Z30AUG	120	Gangneung	12
2003	linfa	00Z31MAY	18Z29MAY	88	Jangheung	30
2003	soudelor	06Z19JUN	00Z18JUN	88	Seogwipo	30
2003	etau	06Z08AUG	00Z07AUG	70	Cheonan	30
2003	maemi	12Z12SEP	18Z11SEP	142	Goheung	18
2004	mindulle	12Z04JUL	12Z03JUL	155	Gwangju	24
2004	megi	00Z19AUG	00Z18AUG	208	Jangheung	24
2004	songda	00Z07SEP	00Z06SEP	46	Ulleungdo	24

Table 5-2 Same as Table 5-1, except for non-AIP cases.

Year	TC name	LFT	T0
1993	ofelia	06Z27JUL	06Z26JUL
1994	walt	00Z26JUL	00Z25JUL
1994	brendan	00Z01AUG	00Z31JUL
1994	ellie	18Z13AUG	18Z12AUG
1994	seth	18Z11OCT	18Z10OCT
1996	eve	12Z18JUL	12Z17JUL
1997	rosie	00Z27JUL	00Z26JUL
1997	oliwa	06Z16SEP	06Z15SEP
1998	zeb	06Z17OCT	06Z16OCT
1999	neil	06Z27JUL	06Z26JUL
1999	paul	06Z07AUG	06Z06AUG
2000	prapiroon	12Z31AUG	12Z30AUG
2002	rammasun	00Z06JUL	00Z05JUL
2002	nakri	12Z13JUL	12Z12JUL
2002	fengshen	12Z26JUL	12Z25JUL
2004	namtheun	00Z01AUG	00Z31JUL
2004	chaba	06Z30AUG	06Z29AUG

5.1.2. Statistical properties

In this subsection, we present the statistical properties of both groups. Analysis time of each AIP case is when the 6-hr precipitation amount was the largest during the antecedent period. On average, the maximum 6-hr precipitation reached about 115.5 mm (6 hr)−1, which exceeds the heavy rain advisory of ≥80 mm (12 h)−1 by the KMA (Table 5-1). The average gap between the analysis time and the landfall time is about 27 hr; in other words, the AIP tended to occur about one day before the TC made its landfall on the peninsula. Thus, the analysis time of the non-AIP case is chosen as one day before the landfall time as well, for a fair comparison between the two cases. The AIP occurrence is likely to have seasonal preference (Table 5-3). A monthly ratio of AIP occurrence gradually increased from July to September, excluding May and June that had just one case. It is likely that the activity of midlatitude synoptic waves increases in the autumn season with an enhancement of the East Asian trough.

The tracks of the two cases (i.e., AIP and non-AIP cases) are shown in Fig. 5-3. For both cases, most TCs recurved in the ocean south of the Korean Peninsula, with more exceptions for the non-AIP cases. It is noted that the tracks for the AIP cases were more concentrated and followed similar pathways, while those for the non-AIP cases are more spread-out. At the analysis time, the TC centers of the most AIP cases were around 28.5°N, which implies that the composite analysis is suitable for the AIP cases. The mean R15 of the AIP cases (non-AIP cases) is about 271 nautical miles (247 nm), and the TC sizes of the AIP cases are slightly bigger than those of the non-AIP cases.

Note that the Korean Peninsula is not included within the mean effective radius.

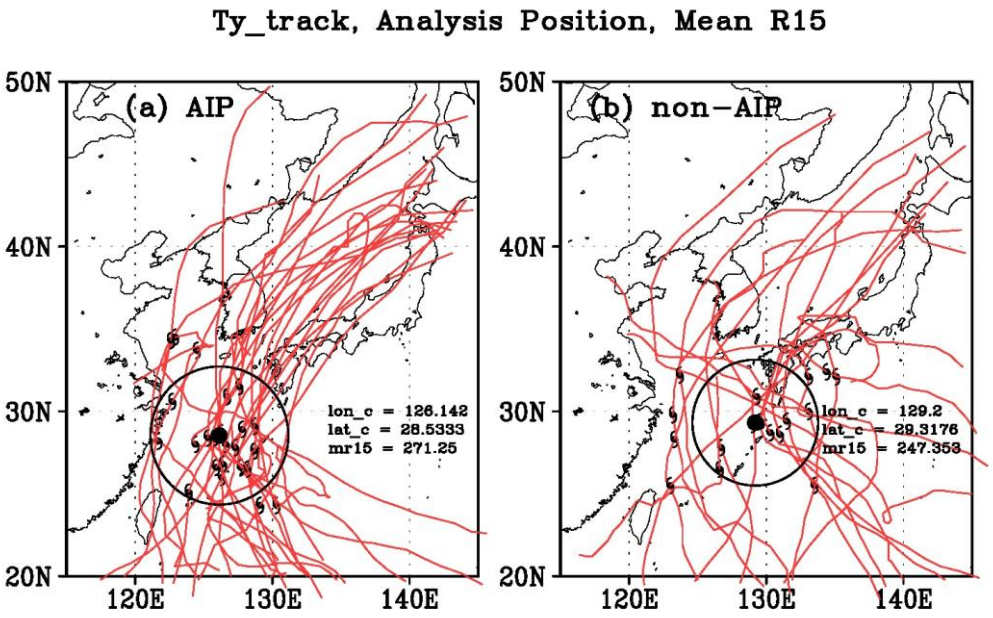

Fig. 5-3 Locations (black TC symbols) and tracks (red line) of the TCs at the analysis time for (a) the AIP case and (b) non-AIP case. Black point and black circle denote mean location and mean effective size for each case, respectively.

Table 5-3. The number of monthly occurrence of AIP and non-AIP cases.

	May	Jun	Jul	Aug	Sep	Oct	Total
AIP	1	1	4	10	8	0	24
nAIP	0	0	9	5	1	2	17
Total	1	1	13	15	9	2	41
Ratio of occurrence of AIP (%, AIP/Total)	100	100	30.8	66.7	88.9	0	58.5

5.1.3. Composite synoptic background

In order to examine the factors that led to the differences between the two cases, we check the synoptic background of each case. Fig. 5-4 compares the composites of synoptic environments at 200, 500, and 850 hPa at the analysis time of the two cases. At 200 hPa, an upper-level trough was commonly observed over mainland China between 110°–120°E for both cases, which contributed to the TC recurvature (Figs. 5-4a, b). However, the trough for the AIP cases was slightly stronger than that for the non-AIP cases, with more intense and statistically more robust jet stream reaching 40 m s−1. Therefore, the AIP cases had stronger baroclinicity over the Korean Peninsula, which is located east of the trough and equatorward of the jet entrance. This facilitates the synoptic-scale ascent that can organize convection and provide a favorable condition for the AIP event.

In addition, the mid-level flow patterns are quite different in terms of the positions of trough and subtropical high (Figs. 5-4c, d). In the AIP cases, the trough intruded into the Yellow Sea and the westerlies of the preexisting midlatitude trough confront with southerlies between the TC and subtropical high. The flow pattern produced a strong horizontal confluent field around the peninsula, which induced relatively stronger temperature and moisture gradients because the warm and moist air from the TC confronted the cold, dry air from the midlatitude trough. In the non-AIP cases, the trough remained over China and the subtropical high expanded further to the peninsula. The confluent flow was located near Japan and its strength was relatively weak.

Therefore, the temperature gradient over the peninsula was also weak.

At the lower level, the trough disappeared west of the peninsula in both cases (Figs. 5-4e, f). For the non-AIP cases, the anticyclonic flow related to the subtropical high expanded further toward the peninsula, compared to the AIP cases. As a result, the southerly flow on the eastern periphery of TC did not extend to the peninsula for the non-AIP cases. The predominant anticyclone over the peninsula prevented the northward transport of deep tropical moisture. By contrast, the low-level moist air accompanied by the southerlies on the east side of TC reached South Korea for the AIP cases. The effective moisture transport between the TC and the subtropical high is an important factor for AIP over the peninsula, as suggested by previous research (e.g., Wang et al. 2009; Galarneau et al. 2010; Schumacher et al. 2011).

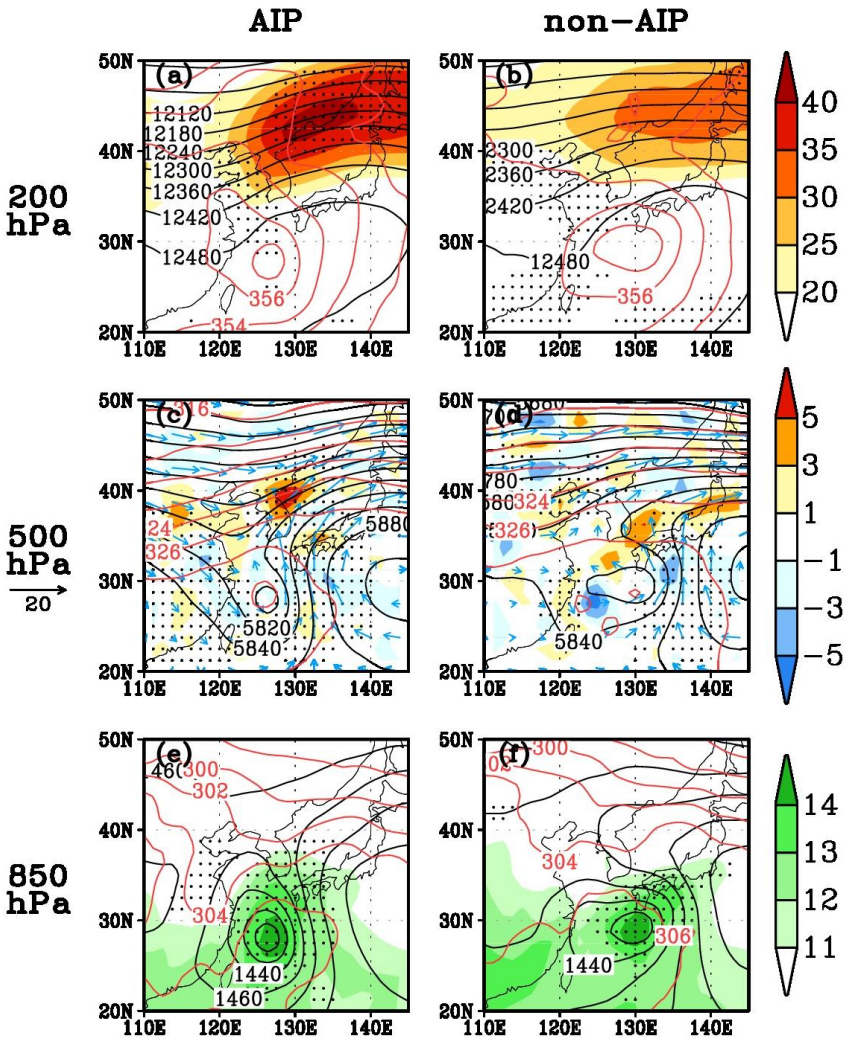

Fig. 5-4 Composite fields of geopotential height (black contours; gpm), temperature (red contours; K) at 200 hPa (a, b), 500 hPa (c, d), and 850 hPa (e, f) for the AIP case (left panels) and non-AIP case (right panels) at their respective analysis times. Shadings represent 200-hPa wind speed (m s^{-1}) in (a, b), 500-hPa convergence (10^{-5} s^{-1}) in(c, d), and 850-hPa relative humidity (%) in (e, f). Dots denote 95% significant region of the shading by Student-*t* test.

5.2 Antecedent frontogenesis for the AIP cases

We suggested that AMF played a critical role in the occurrence of AIP in case and comparison study previously. As shown in Fig. 5-4, the composite synoptic background of the AIP cases shows a favorable environment for generating a frontal structure at the mid level. In this section, the midtropospheric frontogenetical feature will be examined for all the cases and comparison will be made between the two groups. Then, we will generalize the frontogenetical characteristics for the AIP cases and discuss how the front contributed to the precipitation process in the AIP cases.

5.2.1. Case analysis

The TCs approaching the Korean Peninsula encountered the midlatitude trough to their northwest, and the trough was stronger for the AIP cases (Fig. 5-4). To check the robustness of this feature, Fig. 5-5 shows the midtropospheric flows for the six selected AIP cases, vertically averaged from 700 to 400 hPa at the analysis time. The QG frontogenesis functions are also shown to demonstrate the existence of the midtropospheric front. Hereafter, all horizontal maps are shown after being vertically averaged for the whole midtroposphere (700-400 hPa) because the maximum frontogenesis of each case occurred at slightly different levels in the midtroposphere. The flow pattern of each case establishes a horizontal confluent deformation between the midlatitude trough and TC when the southerlies from eastern periphery of TC conflicted with the midlatitude westerlies from the pre-existing upper-level trough.

This flow pattern is a favorable condition for the AMF, as suggested previously. Most cases show the AMF over the Korean Peninsula, which reveals that the front affected the AIP process significantly. For example, in the cases of Bart (1999) (Fig. 5-5b), Saomai (2000) (Fig. 5-5c), and Maemi (2003) (Fig. 5-5e), a line-shaped cloud band was present on the warm side of the frontogenesises, distinctively from the circular convection around the TC (upper panels in Fig. 5-1). A distinctive precipitation outside the effective radius of the TC occurred beneath the cloud shield (middle panels in Fig. 5-1).

The non-AIP cases show a different synoptic environment from the AIP cases, that is, most approaching TCs did not encounter midlatitude trough (Fig. 5-6). These TCs encountered a ridge of synoptic wave or the rear side of the midlatitude trough that was passing by and far away from the TCs. The environment was unfavorable for convergence or deformation over the peninsula to the north of the TCs. As a result, in the non-AIP cases the frontogenesis could not be generated because the TCs did not interact with midlatitude baroclinic environment, which led to direct precipitation by convection at the TC center around landfall time.

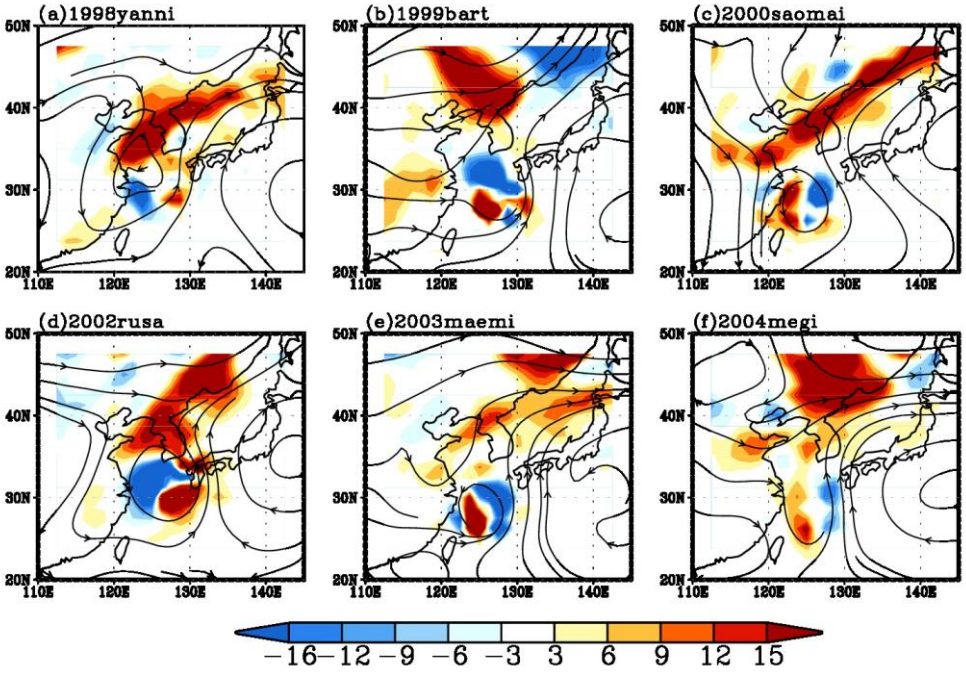

Fig. 5-5 Streamline and QG frontogenesis (shading; K (m s)$^{-1}$) for the six AIP cases averaged between 700 and 400 hPa at the analysis time.

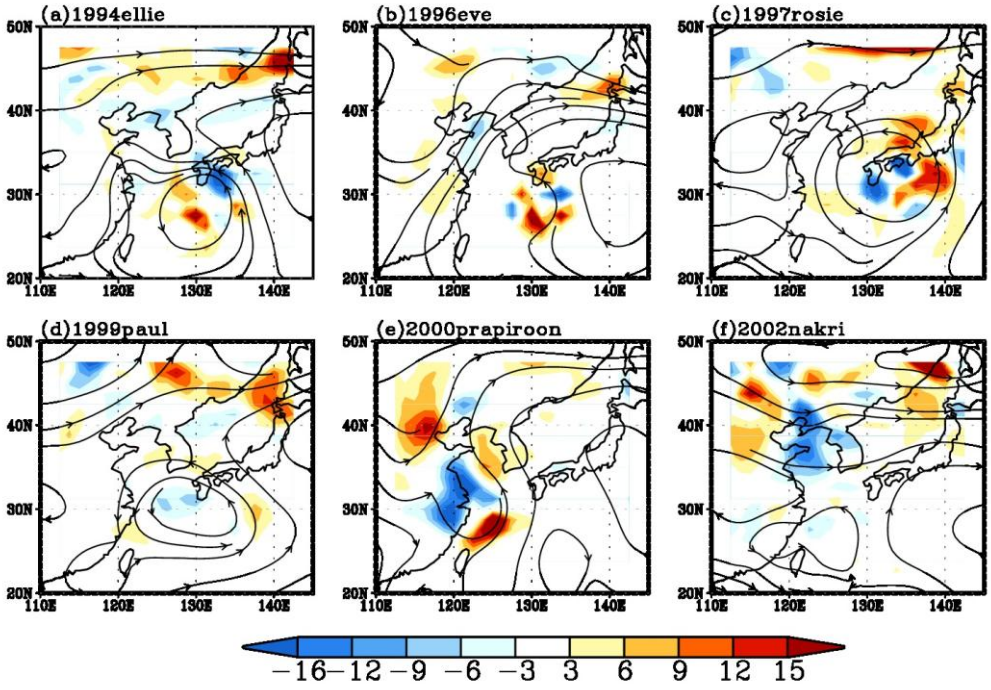

Fig. 5-6 Same as Fig. 5, except for the six non-AIP cases.

5.2.2. Composite analysis

As shown in the previous subsection, the AMF induced by the interaction between TC and midlatitude trough in the AIP cases seems to be linked to the AIP over the Korean Peninsula. To confirm the linkage, QG frontogenesis function is calculated using Eq. (6). This helps to examine how the TC-trough interaction contributed to the generation of a midtropospheric front and to determine how the front influenced the AIP over the Korean Peninsula (Fig. 5-7a). The midtropospheric averaged streamline shows a typical synoptic distribution to make a midtropospheric front between TC and midlatitude trough, i.e., midlatitude trough to the north, TC to the south, and the subtropical high to the east. The QG frontogenesis was generated by confluent and deformed flows between TC-related southerlies and midlatitude trough-related westerlies at the analysis time. The frontal region was elongated from southwest to northeast, which indicates that the ascending motion could be induced on the warm side of the front, i.e., over the AIP region. It is evident that there are two distinctive ascending regions; one is east of the composite TC, and the other is on the warm side of the front over the Korean Peninsula. That implies two important points: (1) The AIP occurred indirectly, apart from the TC, and (2) the upward motion associated with the AMF was highly correlated with the midtropospheric front induced by the interaction between TC and the flow associated with the midlatitude trough. This feature is consistent with the results of case study on Typhoon Rusa (2002) and Maemi (2003).

Q-vector is a useful tool to diagnose how QG frontogenesis leads to ascent in the

frontal region (Martin et al. 1997). From Eq. (7), positive frontogenesis ($\frac{1}{|\nabla_p \theta|}\vec{Q} \cdot \nabla_p \theta$) causes the Q-vector to turn toward the warm side of the front (Fig. 5-7b). The forcing for ascent that was represented by convergence of $\vec{Q}$ ($\nabla \cdot \vec{Q}$) occurs apparently on the warm side of the front over the Korean Peninsula. The distributions of that reveal that the region of midtropospheric QG forcing between the composite trough and the composite TC is in agreement with the ascending region over the Korean Peninsula (Fig. 5-7a). However, it is noted that the regions of the convergence of $\vec{Q}$ and upward motion are slightly different. The convergence of $\vec{Q}$ is formed on the western peninsula, while the strong ascending region covers the entire peninsula. The possible reason of this difference is because the Q-vector is a dynamical indicator without considering diabatic heating in a QG system. Thus, it is natural that it cannot fully explain the actual upward motion.

In order to supplement the problem, the QG omega equation of Eq. (8), including the diabatic heating term, was computed (Fig. 5-8). It enables us to quantitatively examine the distribution of upward motion related to the AMF, shown as the negative omega region over the peninsula in Fig. 5-7a. In the AIP cases, the QG omega equation well represents the omega in terms of spatial pattern and magnitude, i.e., the 3-D Laplacian of composite omega on the left-hand side of Eq. (8) (Fig. 5-8a) is almost equivalent to the sum of geostrophic forcing and diabatic forcing on the right-hand side of the equation (Fig 5-8b).

The vertical motion might be explained by a synergistic interaction between dynamics and thermodynamics. It is reasonable to refer to the process associated with QG forcing as dynamics and the process related to convective heating conditions as thermodynamics. The sum of two QG forcings (i.e., differential geostrophic vorticity advection and the Laplacian of potential temperature advection) describes the spatial pattern of the convergence of $\vec{Q}$ (Fig. 5-7b) because of the relation between the two:

$$-f_0 \frac{\partial}{\partial p}\left[-\vec{V}_g \cdot \nabla\left(\frac{1}{f_0}\nabla^2\Phi + f\right)\right] - \nabla^2\left[-\vec{V}_g \cdot \nabla\left(-\frac{\partial\Phi}{\partial p}\right)\right] = -2\nabla \cdot \vec{Q}. \quad (9)$$

Generally, the magnitude of diabatic forcing is bigger than that of dynamic forcing, mainly due to precipitation and cloudiness in a rainfall event (Martin et al., 1997). Over the Korean Peninsula, the magnitude of QG forcing is also relatively smaller than that of diabatic heating term. However, the QG forcing is as important as the diabatic heating for the upward motion because the latent heat may not be released without condensation through vertical motion. Here, front–precipitation feedback can be suggested for the ascending motion of the AIP cases over the peninsula. First, the upward motion on the warm side of the QG front induces the precipitation over the peninsula. Second, the precipitation causes the diabatic heating due to condensational latent heat. Finally, the diabatic heating forcing again intensifies the upward motion. Meanwhile, the entire vertical motion east of the composite TC is likely induced by the diabatic heating mainly due to latent heat release.

The QG frontogenetical forcing is divided into differential geostrophic vorticity advection (Fig. 5-8e) and the Laplacian of potential temperature advection (Fig. 5-8f). In the AIP cases, the upper-level trough intruded into the northwest of the peninsula while any low-pressure system did not exist at the lower level (Fig. 5-4). The different flow patterns at different vertical levels produced positive differential geostrophic vorticity advection over the region of interest. The potential temperature advection occurred due to the southerlies originated by TC outflow. As a result, the upward motion by QG forcing was induced by the interaction between TC and upper-level trough.

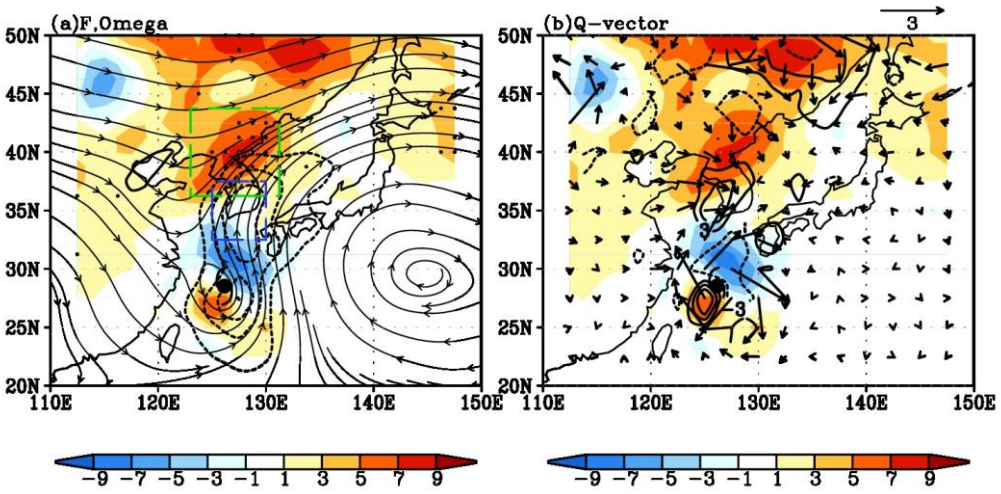

Fig. 5-7 Composite horizontal fields of (a) QG frontogenesis (shading; 10^{-11} K (m s)$^{-1}$), streamline, and omega (contour; -1 Pa s^{-1}) averaged between 700 and 400 hPa, and (b) $\vec{Q} \cdot \nabla_p \theta$ (shading; 10^{-16} K^2 m^{-2} s^{-1}, $\vec{Q}$ (vector, K (m s)$^{-1}$), $\vec{Q}$ convergence (contour; K m^{-2} s^{-1}) at the analysis time. Dashed green (blue) rectangular indicates frontal (ascending) region, which will be used for area-averaged correlation (see the text). Dots denote 95% significant region of the shading by Student-*t* test. The TC symbol indicates the composite TC location.

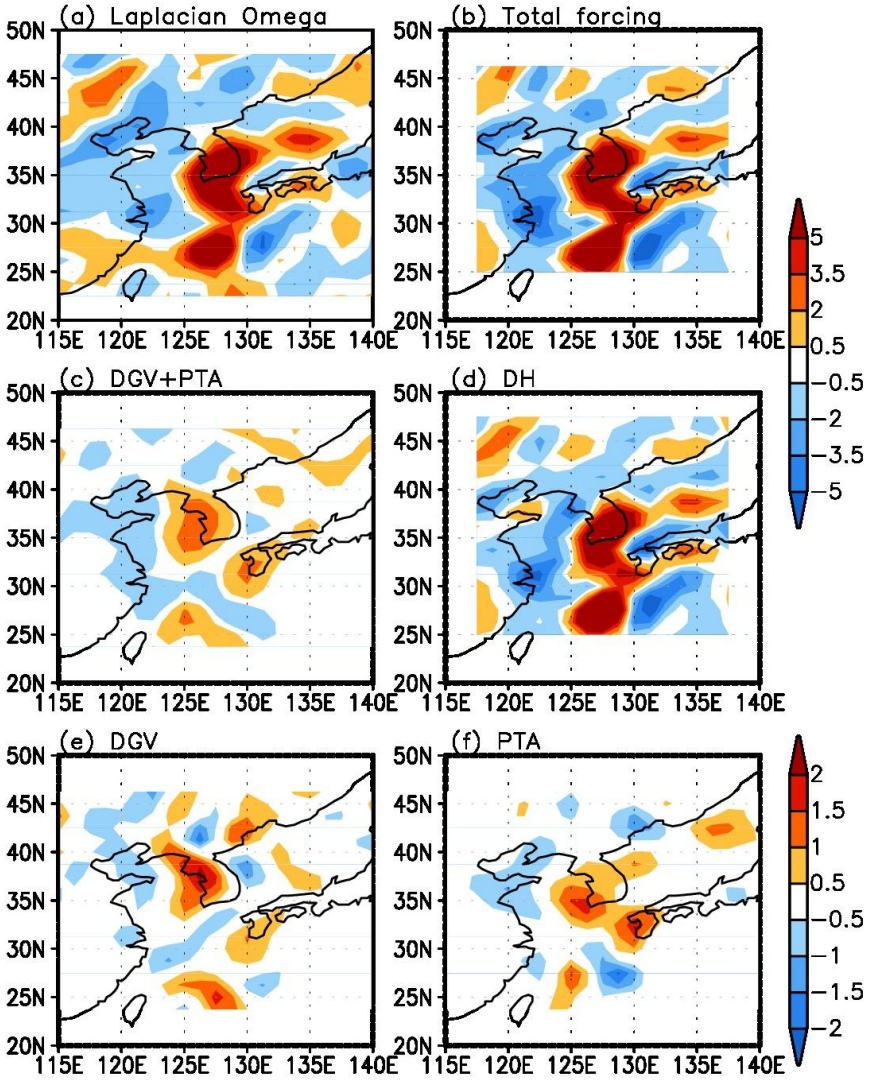

Fig. 5-8 Composite analysis of QG omega equation averaged between 700 and 400 hPa. (a) Three-dimensional Laplacian of composite omega (LHS of eq. (3)), (b) sum of all forcing terms (RHS of eq. (3)), (c) sum of QG forcing terms, (d) diabatic forcing terms, (e) differential geostrophic vorticity advection term, and (f) the Laplacian of potential temperature advection term. The units of all panels are 10^{-12} Pa m^{-2} s^{-1}.

5.2.3. Precipitation process

Many researchers have investigated antecedent rainfall events of TCs (e.g., Stohl et al. 2008; Wang et al. 2009; Chen et al. 2010; Galarneau et al. 2010; Schumacher et al. 2011). They noted that deep moisture is a key element for heavy rainfall. In general, when a TC entered the midlatitude baroclinic environment, poleward moisture transport at the lower level was caused by outflows of the TC. In the AIP cases, however, strong moisture flux was also converged around the frontal region in midtroposphere (Fig. 5-9a). The southerlies between TC and the subtropical high reach the Korean Peninsula, and then pumped abundant moisture of tropical region into midlatitude. In the cross section along the cross-frontal line (i.e., 127.5°E isogradient), the meridional moisture flux convergence occurred in the northern periphery of TC near the surface as well as at midtroposphere on the warm side of the front due to confluence of the AMF (Fig. 5-9b). It indicates that the midtropospheric ascent induced by the front could produce an abundant precipitation with sufficient moisture supply to the midtroposphere.

The major frontogenesis occurred at the midtropospheric levels from 700 to 400 hPa above the Korean Peninsula, with a relatively strong gradient of potential temperature (Fig. 5-10). A strong ascent on the warm side of the midtropospheric front existed at mid levels, distinctively away from the TC center (28°N), which implies that two precipitation events (i.e., the first is AIP and the second is direct precipitation of TC) occurred over the peninsula when TC approaching. Induction of thermally direct

circulation can be expected with a positive frontogenesis function in the midtroposphere (e.g., Martin et al. 1992). This thermally direct circulation intensified the convection over the frontal region ahead of the TC, which caused the AIP over the Korean Peninsula.

Scatter plots in Fig. 5-11 demonstrate the linear relationship among the frontogenesis, ascent, and precipitation at the analysis time for the AIP cases. We can interpret the linear relation between precipitation and midtropospheric ascent, which has a high correlation of above 0.7 (Fig. 5-11a). Note that the correlation between the QG frontogenesis north of the peninsula and the ascent over the peninsula is above 0.5 (Fig. 5-11b). This implies that the frontogenesis can lead the ascent over the peninsula through the front–precipitation feedback process as suggested above, resulting in a correlation over 0.5 between the frontogenesis and the AIP. The AMF is likely to have a role in producing the precipitation during antecedent time prior to the TC landfall.

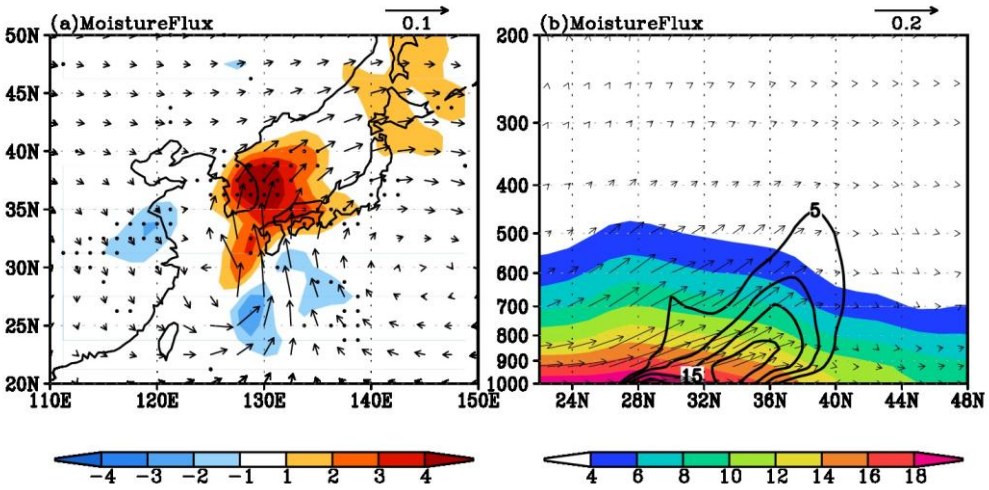

Fig. 5-9 Composite of (a) moisture flux (vector; m s^{-1}) and moisture flux convergence (shaded; m^{-2} s^{-1}) averaged between 700 and 400 hPa at the analysis time, (b) cross-section of specific humidity (shading; g kg^{-1}), vertical moisture flux by meridional wind components (m s^{-1}) and negative pressure velocity (30 × Pa s^{-1}) along 127.5E isogradient. Dots denote 95% significant region of the shading by Student-*t* test.

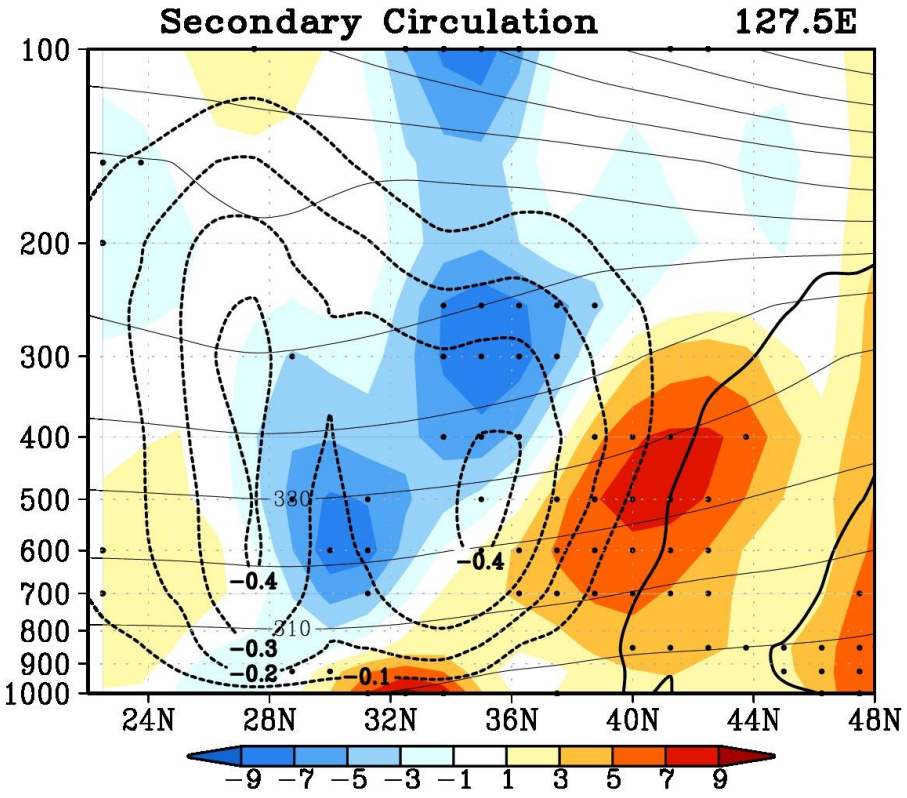

Fig. 5-10 Vertical cross-sections of total frontogenesis (10^{-11} K m^{-1} s^{-1}; shading), potential temperature (contours; K), and pressure velocity (Pa s^{-1}) along 127.5E isogradient. Dots denote 95% significant region of the shading by Student-*t* test.

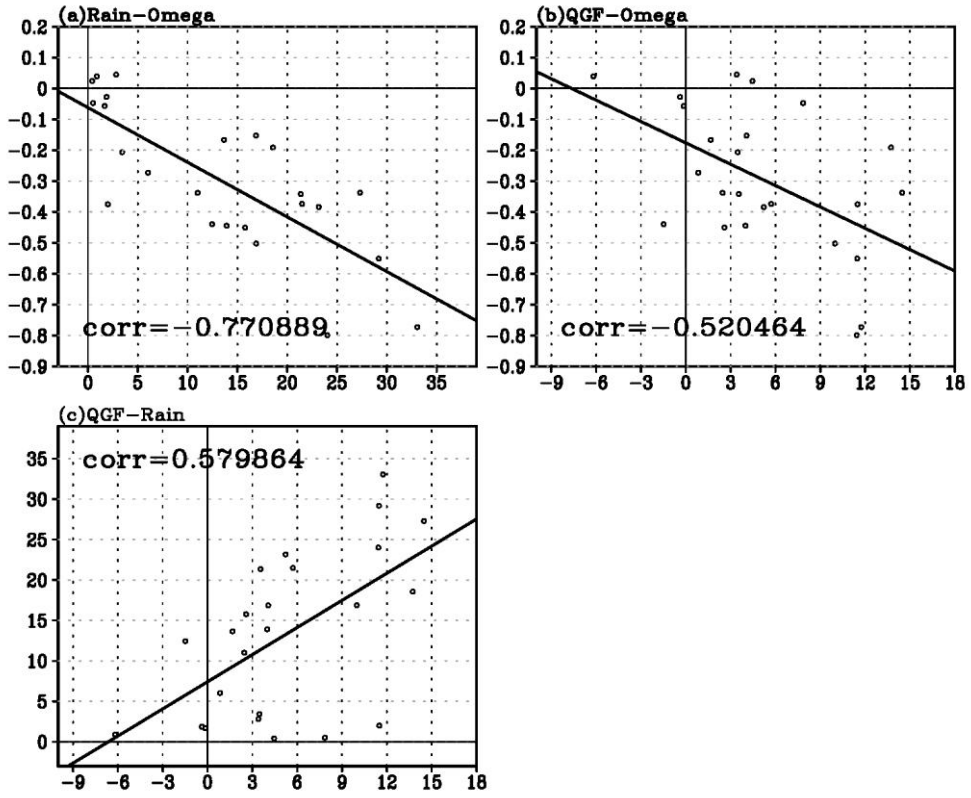

Fig. 5-11 Scatter plot and correlation for the relationship (a) between precipitation averaged using all the stations on the peninsula and pressure velocity averaged over the ascending region (blue box in Fig. 5-7a), (b) between QG Frontogenesis averaged over the frontal region (green box in Fig. 5-7a) and pressure velocity, and (c) between QG frontogenesis and precipitation at each analysis time.

6. Summary and Concluding Remarks

We demonstrate that the AMF occurred across the middle part of the Korean Peninsula with its maxima and contributed to the AIP ahead of TC. For the objective, we carried out 3 research topics, i.e., case study, comparison study, and statistical analysis.

First, we examined antecedent midtropospheric frontogenesis (AMF) resulting from the interaction between Typhoon Rusa (2002) and a midlatitude trough over the Korean Peninsula. The existence of the AMF was confirmed by three observational evidences: 1) the distinguishable convective cloud band in the middle province of the peninsula from the enhanced IR images, 2) the strong horizontal confluent deformation and the tightened temperature gradient at the mid-troposphere with strong vertical wind shear to the northeast of the peninsula, and 3) the distinctively saturated layer near 500 hPa from the proximate vertical sounding. Based on these observational evidences, the AMF was simulated by the high-resolution WRF/ARW model. The ascent on the warm side of the front showed that the AMF played a role in the development of the first heavy rainfall event in Gangneung with a strong MFC at the mid-level. The ascent on the warm side of the AMF resulted in the wide spread saturation above Gangneung with relatively high hydrometeor contents on the warm side of the front that was distinctive from the low-level saturation. The trajectory of the mid-level air parcel showed that the moisture relevant to the AMF was originated from the mid-level of the subtropical ocean by southerlies along the eastern flank of the TC.

We further calculated the three contributing terms (i.e., the HDF, TF, and DF) to the total frontogenesis for the AMF during the time period of the first rainfall event in Gangneung with the simulated data. The horizontal and temporal features of the terms indicate that the AMF was mainly forced by the HDF which was generated by the deformed and confluent flows between the warm southerlies originating from the TC and the cold northwesterlies induced by the midlatitude trough at the mid-level. Although the absolute magnitudes of the TF and DF related to the vertical motion were found to be larger than that of the HDF, these two terms largely offset each other. The AMF occurred ahead of the TC prior to the ET process with the different vertical structure from that of the ETF. The thermally direct circulation associated with the AMF lead to the midtropospheric saturation, which enhanced the precipitation of the first rainfall event together with the orographically forced convection at the low-level above Gangneung.

Second, we also investigated favorable synoptic environments for AIP ahead of TC through comparison of two TCs, Rammasun (2002) and Maemi (2003). While their recurving latitudes, landfall points, and effective sizes were different, the two TCs were similar in that they approached the peninsula from a similar direction and had a remarkably similar accumulated rainfall pattern over the period. However, the temporal evolutions of their hourly rainfall were quite different in the region (i.e., the Jiri Mountains) that experienced the maximum accumulated rainfall. While just one rainfall maximum was found associated with Rammasun, two maximums were observed during the approach of Maemi. The satellite derived rainfall and enhanced IR

cloud images revealed that the first rainfall maximum associated with Maemi was an AIP that was related to a frontal structure. These features imply the important role of TC–midlatitude trough interaction in causing the AIP.

When a TC interacts with a midlatitude trough to its north as in the Maemi case, the confluent flows at mid-levels are enhanced due to increased pressure gradient in the midst of the TC, subtropical high, and midlatitude trough, and the warm advection associated with the confluent flows also becomes stronger near the confluent zone. Analysis of the three-dimensional frontogenesis equation revealed that the HDF generated by the confluent flows contributed positively to frontogenesis. However, the DF and TF terms related to vertical motion largely offset each other, though their individual magnitudes were larger than that of the HDF. The abundant low-level moisture supply by the southerly wind on the east side of Maemi was also a critical factor for the intense AIP. Frontogenesis is associated with a thermally-direct secondary circulation that acts to restore thermal wind balance by increasing the vertical wind shear and reducing the temperature gradient. For the Maemi case, an elongated region of ascent on the warm side of the front was likely associated with the ascending vertical branch of the secondary circulation, thereby providing the linkage between frontogenesis and the organization of convection in a warm and moist environment.

Finally, we found that many cases showed double precipitation peaks, including the AIP, associated with TCs that were approaching the Korean Peninsula. AMF induced by the interaction between TC and midlatitude trough was examined in terms of the

physical processes for the AIP occurrence over the Korean Peninsula. In this study, a set of 41 cases that affected the Korean Peninsula was collected for the period from 1993 to 2004 based on the Typhoon White Book (2011) issued by the KMA, and they were classified into the AIP and non-AIP cases. About 60% of the total TC cases were defined as the AIP cases, and the maximum 6-hr precipitation reached about 115.5 mm $(6\ hr)^{-1}$. The AIP occurred about one day before the TC made its landfall on the peninsula. In the AIP cases, the synoptic background shows that approaching TC encountered the downstream side of the pre-existing midlatitude trough, resulting in the formation of the confluent frontal region. At that time, the Korean Peninsula lay on the equatorward of the jet entrance and was subject to warm, moist air due to southerlies from the TC. In contrast, in the non-AIP cases, the trough remained over China and the subtropical high expanded to the peninsula so that the TC's outflow did not reach the peninsula.

For the AIP cases, midtropospheric QG frontogenesis occurred significantly in and around the Korean Peninsula, which did not happen in the non-AIP cases. The warm, moist air conveyed from the TC impinged upon the cold, dry air from northeastern China in the midtroposphere, which resulted in the AMF over the Korean Peninsula. Composite analyses of the AIP cases were conducted to generalize the frontogenetical mechanism and to evaluate the AIP induced by the front. The QG frontogenesis induced by the interaction between TC and midlatitude upper-level trough caused the convergence of $\vec{Q}$ on the warm side of the front with accompanying upward motion. The QG omega equation analysis indicated that the ascending motion of the AMF was

attributed to the sum of QG forcing and diabatic forcing by front–precipitation feedback. In addition, the QG frontogenetical forcing consisted of differential geostrophic vorticity advection by upper-level trough and the Laplacian of potential temperature advection by TC. A sufficient moisture flux convergence reached the mid level as well as the lower level because of confluence over the frontal region. The thermally direct circulation induced by the front intensified the convection with abundant moisture over the frontal region apart from the TC, which caused the AIP of the Korean Peninsula. Fig. 6.1 shows clearly the essential features as the schematic diagram

To sum up, this study showed that the AIP occurred ahead of TC in many cases and was highly correlated with the midtropospheric frontogenesis induced by the interaction of TC and midlatitude trough. We expect that our results can provide useful information to forecast the location and amount of the AIP ahead of the TC approaching the Korean Peninsula.

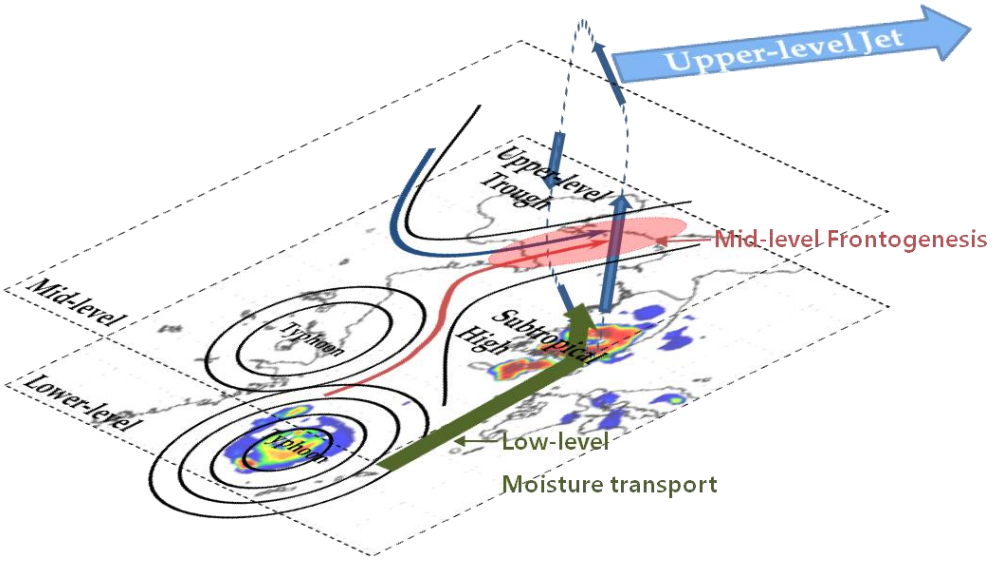

Fig 6-1 Schematic diagram for the AIP over the Korean Peninsula associated with mid-tropospheric frontogenesis. The shading at lower level is precipitation rate at the analysis time, and the green arrow indicates the low-level moisture transport. The blue (red) curved arrow at mid level denotes cold (warm) air from the upper-level trough (TC). The dashed box with blue arrows illustrates a thermally direct (secondary) circulation induced by the frontogenesis.

References

Agustí-Panareda, A., C. D. Thorncroft, G. C. Craig, and S. L. Gray, 2004: The extratropical transition of Hurricane Irene (1999): A potential vorticity perspective. *Quart. J. Roy. Meteor. Soc.*, **130**, 1047-1074.

Agustí-Panareda, A., S. L. Gray, G. C. Craig, and C. D. Thorncroft, 2005: The extratropical transition of Tropical Cyclone Lili (1996) and its crucial contribution to a moderate extratropical development. *Mon. Wea. Rev.*, **133**, 1562-1573.

Atallah, E. H., L. F. Bosart, and A. R. Aiyyer, 2007: Precipitation distribution associated with landfalling tropical cyclones over the eastern United States. *Mon. Wea. Rev.*, **135**, 2185-2206.

Anwender, D., P. A. Harr, and S. C. Jones, 2008: Predictability Associated with the Downstream Impacts of the Extratropical Transition of Tropical Cyclones: Case Studies. *Mon. Wea. Rev.*, **136,** 3226–3247.

Ballentine, R. J., 1980: A numerical investigation of New England coastal frontogenesis. *Mon. Wea. Rev.*, **108,** 1479–1497.

Bluestein, H. B. 1993. Synoptic-Dynamic Meteorology in Midlatitudes, vol. 2, Observations and Theory of Weather Systems. 253 pp., *Oxford Univ. Press*, New York.

Bryan, G. H., and M. J. Fritsch, 2000: Diabatically driven discrete propagation of

surface fronts: A numerical analysis. *J. Atmos. Sci.,* **57,** 2061–2079.

Byun, K. –Y., and T. –Y. Lee, 2012: Remote effects of tropical cyclones on heavy rainfall over the Korean peninsula – statistical and composite analysis. *Tellus*, **64**, 14983, doi: 10.3402/tellusa.v64i0.14983

Chen, L., Y. Li, and Z. Cheng, 2010: An overview of research and forecasting on rainfall associated with landfalling tropical cyclones. *Adv. Atmos. Sci.*, **27(5)**, 967–976.

Chien, F.-C., and H.-C. Kuo, 2011: On the extreme rainfall of Typhoon Morakot (2009). *J. Geophys. Res.*, **116**, D05104, doi:10.1029/2010JD015092.

Cordeira, Jason M., Lance F. Bosart, 2011: Cyclone interactions and evolutions during the "Perfect Storms" of late October and early November 1991. *Mon. Wea. Rev*., **139**, 1683-1707.

Doswell, C. A., III, 1984: A kinematic analysis of frontogenesis associated with a nondivergent vortex. *J. Atmos. Sci.,* **41,** 1242–1248.

Doswell, C. A., 1985: Reply. *J. Atmos. Sci.,* **42,** 2076–2079.

Dudhia, J., 1989: Numerical study of convection observed during the winter monsoon experiment using a mesoscale two-dimensional model. *Atmos. Sci.*, **46**, 3077-3107.

Galarneau, T. J., Jr., L. F. Bosart, C. A. Davis, and R. McTaggart-Cowan, 2009: Baroclinic transition of a long-lived mesoscale convective vortex. *Mon. Wea.*

Rev., **137**, 562–584.

Galarneau, T. J., Jr., L. F. Bosart, and R. S. Schumacher 2010: Predecessor rain events ahead of tropical cyclones. *Mon. Wea. Rev.*, **138**, 3272–3297.

Hanley, D., Molinari, J., and Keyser, D., 2001: A composite study of the Interaction between tropical cyclones and Upper-Tropospheric Troughs. *Mon. Wea. Rev.*, **129,** 2570–2584.

Harr, P. A., and R. L. Elsberry, 2000: Extratropical transition of tropical cyclones over the western North Pacific. Part I: Evolution of structural characteristics during the transition process. *Mon. Wea. Rev.,* **128,** 2613–2633.

_____, _____, and T. F. Hogan, 2000: Extratropical transition of tropical cyclones over the western North Pacific. Part II: The impact of midlatitude circulation characteristics. *Mon. Wea. Rev.*, **128,** 2634–2653.

_____, D. Anwender, and S. C. Jones, 2008: Predictability Associated with the Downstream Impacts of the Extratropical Transition of Tropical Cyclones: Methodology and a Case Study of Typhoon Nabi. *Mon. Wea. Rev.,* **136,** 3205–3225.

Hart, R. E., J. L. Evans, and C. Evans, 2006: Synoptic conditions of the extratropical transition life cycle of North Atlantic tropical cyclones: Factors determining posttransition evolution. *Mon. Wea. Rev*., **134**, 553-578.

Hong, S. –Y., J. Dudhia, and S. –H. Chen, 2004: A Revised Approach to Ice

Microphysical Processer for the Bulk Parameterization of Clouds and Precipitation. *Mon. Wea. Rev.*,555 **132**, 103-120.

_____, Y. 556 Noh, and J. Dudhia, 2006: A New Vertical Diffusion Package with an Explicit Treatment of Entrainment Processes. *Mon. Wea. Rev.*, **134**, 2318-2341.

_____, and J.-O. Lim, 2006: The WRF single-moment 6-class microphysics scheme (WSM6). *J. Korean Meteor. Soc.*, **42**, 129–151.

Jones, S. C., P. A. Harr, J. Abraham, L. F. Bosart, P. J. Bowyer, J. L. Evans, D. E. Hanely, B. N. Hanstrum, R. E. Hart, F. Lalaurette, M. R. Sinclair, R. K. Smith, and C. Thormcroft: The Extratropical transition of tropical Cyclones: Forecast challenges, current understanding, and future directions. *Wea. Forecasting*, **18,** 1052–1092.

Kang, J., 2004: The mechanism of heavy rainfall near Gangneung associated with Typhoon Rusa (2002). M.S. thesis, Dept. of Atmospheric Sciences, Yonsei Univericity, Seoul, Korea.

Kain, J. S., and J. M. Fritsch, 1990: A one-dimensional entraining/ detraining plume model andits application in convective parameterization. *J. Atmos. Sci.*, **47**, 2748-2802.

_____, and _____, 1993: Convective parameterization for mesoscale models: The Kain-Fritcsh scheme. *The representation of cumulus convection in numerical models*, K. A.Emanuel and D. J. Raymond, Eds., Amer. Meteor. Soc., 246pp.

Keyser, D., M. J. Reeder, and R. J. Reed, 1988: A generalization of Petterssen's frontogenesis function and its relation to the forcing of vertical motion. *Mon. Wea. Rev.,* **116,** 762–780.

Kitabatake, N., 2001: Extratropical transformation of Typhoon Vicki (9807): Structural change and the role of upper-tropospheric disturbances. *J. Meteor. Soc. Japan,* **80,** 229-247.

_____, 2008: Extratropical Transition of Tropical Cyclones in the Western North Pacific:Their Frontal Evolution. *Mon. Wea. Rev.,* **136,** 2066–2090.

Klein, P. M., P. A. Harr, and R. L. Elsberry, 2000: Extratropical transition of western North Pacific tropical cyclones: An overview and conceptual model of the transformation stage. *Wea. Forecasting,* **15,** 373–395.

Koch, S. E., J. T. McQueen, and V. M. Karyampudi, 1995: A numerical study of the effects of differential cloud cover on cold frontal structure and dynamics. *J. Atmos. Sci.,* **52,** 937–964.

Lee, D.-K., and S.-J. Choi, 2010: Observation and numerical prediction of torrential rainfall over Korea caused by Typhoon Rusa (2002). *J. Geophys. Res.*, **115**, D12105, doi:10.1029/2009JD012581.

Lin, Y. L., D. B. Ensley, S. Chiao, and C.-Y. Huang (2002), Orographic influences on rainfall and track deflection associated with the passage of a tropical cyclone, *Mon. Weather Rev.*, 130, 2929–2950.

Locatelli, J. D., M. T. Stoelinga, and P. V. Hobbs, 2002b: Organization and structure of clouds and precipitation on the mid-Atlantic coast of the United States. Part VII: Diagnosis of a nonconvective rainband associated with a cold front aloft. *Mon. Wea. Rev.*, **130,** 278–297.

Marks, F. D., Jr., 1985: Evolution of the structure of precipitation in Hurricane Allen (1980). *Mon. Wea. Rev.*, **113**, 909–930.

Martin, J. E., J. D. Locatelli, and P. V. Hobbs, 1992: Organization and structure of clouds and precipitation on the mid-Atlantic coast of the United States, Part V: The role of an upper-level front in the generation of a rainband. *J. Atmos. Sci.*, **49**, 1293-1303.

Merrill, J. T., R. Bleck, and D. Boudra, 1986: Techniques of Lagrangian trajectory analysis in isentropic coordinates. *Mon. Wea. Rev*., **114**, 571-581.

Mlawer, E. J., S. J. Taubman, P. D. Brown, M. J. Iacono, and S. A. Clough, 1997: Radiative transfer for inhomogeneous atmosphere: RRTM, a validated correlated-k model for the longwave. *J. Geophys. Res.*, **102** (D14), 16663-16682.

Moore, Richard W., Michael T. Montgomery, 2005: Analysis of an idealized, three-dimensional diabatic Rossby vortex: A coherent structure of the moist baroclinic atmosphere. *J. Atmos. Sci*., **62**, 2703-2725.

Novak, David R., Lance F. Bosart, Daniel Keyser, Jeff S. Waldstreicher, 2004: An observational study of cold season-banded precipitation in Northeast U.S.

cyclones. *Wea. Forecasting*, **19**, 993-1010.

Orlanski, I., B. Ross, L. Polinsky, and R. Shaginaw, 1985: Advances in the theory of atmospheric fronts. *Advances in Geophysics,*Academic Press, 223–252.

Park, S. K., and E. Lee, 2007: Synopitc features of orographically enhanced heavy rainfall on the east coast of Korea associated with Typhoon Rusa (2002). *Geophys. Res. Lett.*, **34**, L02803, doi:10.1029/2006GL028592.

Peng, M. S., and S. W. Chang, 2002: Numerical Forecasting Experiments on Typhoon Herb (1996). *J. Meteor. Soc. Japan*, **80**, 1325-1338.

Ritchie, E. A., and R. L. Elsberry, 2003: Simulations of the Extratropical Transition of Tropical Cyclones: Contributions by the Midlatitude Upper-Level Trough to Reintensification. *Mon. Wea. Rev.*, **131**, 2112-2128

_____, and _____, 2007: Simulations of the Extratropical Transition of Tropical Cyclones: Phasing between the Upper-Level Trough and Tropical Cyclones. *Mon. Wea. Rev.*, **135**, 862-876

Schultz, D. M., and C. A. Doswell III, 1999: Conceptual models of upper-level frontogenesis in southwesterly and northwesterly flow. *Quart. J. Roy. Meteor. Soc.*, **125,** 2535–2562.

Schumacher, R. S., T. J. Galarneau Jr., and L. F. Bosart, 2011: Distant effects of a recurving tropical cyclone on rainfall in a midlatitude convective system: A high-impact predecessor rain event. *Mon. Wea. Rev*., **139**, 650–667.

Shimazu, Y., 1998: Classification of precipitation systems in mature and early weakening stages of typhoons around Japan. *J. Meteor. Soc. Japan*, **76**, 437–445.

Sinclair, M. R., 2002: Extratropical transition of southwest Pacific tropical cyclones. Part I: Climatology and mean structure changes.*Mon. Wea. Rev.,* **130,** 590–609.

Wang, Y., Y. Wang, and H. Fudeyasu, 2009: The role of Typhoon Songda (2004) in producing distantly located heavy rainfall in Japan. *Mon. Wea. Rev.*, **137**, 3699–3716.

Wu, C.-C., 2001: Numerical simulation of Typhoon Gladys (1994) and its interaction with Taiwan terrain using the GFDL hurricane model. *Mon. Wea. Rev.*, **129**, 1533–1549.

Wu, C.-C., T.-H. Yen, Y.-H. Kuo, and W. Wang, 2002: Rainfall simulation associated with Typhoon Herb (1996) near Taiwan. Part I: The topographic effect. *Wea. Forecasting*, **17**, 1001–1015.

Wu, C.-C., K. W. Cheung, and Y.-Y. Lo, 2009: Numerical study of the rainfall event due to the interaction of Typhoon Babs (1998) and the northeasterly monsoon. *Mon. Wea. Rev.*, **137**, 2049–2064.

Appendix A. Sedimentation of hydrometeor contents (SHC)

The vertically integrated water vapor and total hydrometeor contents budgets can be expressed as

$$\frac{\partial[q_v]}{\partial t} = [ADV_{qv}] - [S_{qv}] \qquad (A1)$$

$$\frac{\partial[C]}{\partial t} = [ADV_C] - [SHC] + [S_C], \qquad (A2)$$

where a term in square brackets signifies a mass-weighted vertical integration between two levels (p_1 and p_2) as defined by $[F] = \frac{1}{g}\int_{p_1}^{p_2} F\,dp$ for any variable F. In (A1) and (A2), q_v is the mixing ratio of water vapor and C is the sum of mixing ratios of hydrometeor contents; i.e. cloud water, rain water, cloud ice, snow, and graupel, (ADV_{qv}) and (ADV_C) are three-dimensional advection of water vapor and hydrometeor contents, respectively. S_{qv} and S_c are the source and sink in the water vapor and hydrometeor contents budget due to conversions between water vapor and various hydrometeor species. SHC is total sedimentation of hydrometeor contents, i.e., SHC=$\frac{1}{g}\frac{\partial}{\partial p}(q_C \omega_T)$, where q_C and ω_T are mixing ratio of hydrometeor contents and terminal velocity, due to saturation in specific column. Note that (S_{qv}) = (S_c), when averaged over the specific region. Then (SHC) is expressed as

$$[\mathrm{SHC}] = -\left(\frac{d[q_v]}{dt} + \frac{d[C]}{dt}\right), \qquad \text{(A3)}$$

which means that SHC indicates the fallout residual following an air parcel. The equation (A3) presents the difference between precipitation and evaporation at the surface if the SHC is integrated from the surface to the top of the model;

$$P_s - E_s = -\left\{\frac{d}{dt}\left(\frac{1}{g}\int_{p_s}^{p_t} q_v dp\right) + \frac{d}{dt}\left(\frac{1}{g}\int_{p_s}^{p_t} C dp\right)\right\}, \qquad \text{(A4)}$$

where P_s, E_s, p_s, and p_t denote precipitation, evaporation, surface pressure, and the pressure at the top of the model, respectively.

국문 초록

본 연구는 태풍이 한반도에 접근할 때, 그 전면에서 이전에 발생하는 중층 전선(Antecedent Midtropospheric Frontogenesis, AMF)이 발생하고 그것이 한반도에 태풍 상륙 이전에 발생하는 간접 강수(Antecedent Indirect Precipitation)를 유발함을 밝히고자 한다. 이를 위해 본 연구에서는 3가지 연구 주제, 즉 사례 연구, 비교 연구, 통계적 분석 연구를 수행하였다.

먼저, 본 연구는 2002년 발생한 태풍 루사 사례 연구를 통해 태풍과 중위도 저기압 사이에서 이전 중층 전선(AMF)이 발생했음을 밝혔다. 당시 강릉(37.75°N, 128.90°E)에서는 전체 강수 기간 중 두 개의 강수 피크가 발생하였는데 이 중 첫 번째 피크는 태풍이 상륙하기 약 12시간 전에 AMF에 의해 발생한 이전 간접 강수(AIP) 였다. 중규모 수치 모형(WRF model)을 통해 이러한 AMF는 주로 전선 강제력 중 수평 변형 강제력(horizontal deformation forcing)에 의해 발생되었음을 확인하였다. 이러한 수평 변형 강제력은 태풍으로부터 불어오는 남풍과 중위도 저기압에서 불어오는 북서풍이 만나 발생한 것이다.

두 번째로, 본 연구에서는 어떠한 경우에 AIP가 발생하는지 살펴보기 위해 태풍 라마순(2002)과 태풍 매미(2003), 두 태풍의 종관 배경을 조사해 보았다. 비록 두 태풍의 매우 비슷한 경로와 누적 강수 패턴을 보여 주지만,

지리산 지역의 강수 시계열은 다른 패턴을 보였다. 매미의 경우에서만 태풍 루사와 같은 두 개의 피크를 보여 주었는데, 이는 태풍 매미만이 태풍 전면에서 중층 전선이 발생하였기 때문이다. 이 중층 전선은 태풍에 의한 남풍이 한반도 서쪽 상층 저기압과 태풍 오른쪽에 위치한 아열대 고기압(북태평양 고기압) 사이의 기압 경도력을 강화 시켜, 그 지역에 온도 경도를 강화 시켰기 때문에 발생한 것이다.

마지막으로, 이러한 AIP가 한반도에 얼마나 자주 발생하는지, 또 그 AIP가 AMF에 의한 것인지 일반화 시키기 위해 한반도 영향 태풍들의 통계적 분석을 수행하였다. 본 연구에서는 태풍 백서에서 제공 되는 1993년부터 2004년까지 한반도 영향 태풍 41개를 수집하여, 이를 AIP가 발생한 경우(AIP case)와 그렇지 않은 경우(non-AIP case)로 분류하였다. 이중 약 58%의 태풍이 AIP case로 분류 되었으며, 그 때 발생한 AIP의 강도는 평균적으로 약 105 mm $6h^{-1}$로 매우 강한 강수를 보여 주었다. 컴퍼짓 분석에서 이러한 AMF는 이전 연구와 마찬가지로 태풍과 중위도 저기압 사이의 상호 작용에 의해 발생하였음을 보여주었다. 지균 오메가 함수 분석을 통해, AMF가 AIP의 발생에 상당한 영향을 미쳤음을 밝혔다. 즉 AMF로 인한 열적 직접 순환(Thermally direct circulation)이 AIP 발생시기에 한반도 지역 강한 상승운동을 유발하였고, 이는 하층에서 태풍으로부터의 강한 수분 전달과 함께 태풍 전면에서 AIP를 발생시킨다.